



**O₂ A-band
fluorescence
retrievals**

J. Joiner et al.

This discussion paper is/has been under review for the journal Atmospheric Measurement Techniques (AMT). Please refer to the corresponding final paper in AMT if available.

Global monitoring of terrestrial chlorophyll fluorescence from moderate spectral resolution near-infrared satellite measurements: methodology, simulations, and application to GOME-2

J. Joiner¹, L. Guanter², R. Lindstrot², M. Voigt², A. P. Vasilkov³, E. M. Middleton¹, K. F. Huemmrich⁴, Y. Yoshida³, and C. Frankenberg⁵

¹NASA Goddard Space Flight Center, Greenbelt, MD, USA

²Free University of Berlin, Berlin, Germany

³Science Systems and Applications, Inc., Lanham, MD, USA

⁴University of Maryland, Baltimore County, Joint Center for Environmental Technology (UMBC-JCET), Baltimore, MD, USA

⁵Jet Propulsion Laboratory, California Institute of Technology, Pasadena, CA, USA

Received: 23 March 2013 – Accepted: 12 April 2013 – Published: 22 April 2013

Correspondence to: J. Joiner (joanna.joiner@nasa.gov)

Published by Copernicus Publications on behalf of the European Geosciences Union.

Title Page

Abstract

Introduction

Conclusions

References

Tables

Figures



Back

Close

Full Screen / Esc

Printer-friendly Version

Interactive Discussion



Abstract

Globally mapped terrestrial chlorophyll fluorescence retrievals are of high interest because they can provide information on the functional status of vegetation including light-use efficiency and global primary productivity that can be used for global carbon cycle modeling and agricultural applications. In addition, fluorescence can contaminate photon path estimates from the O₂ A-band that has become an integral part of missions to accurately measure greenhouse gas concentrations. Global mapping of far-red (~ 755–770 nm) terrestrial vegetation solar-induced fluorescence from space has been accomplished using the high spectral resolution ($\nu/\Delta\nu > 35\,000$) interferometer on the Japanese Greenhouse gases Observing SATellite (GOSAT). These satellite retrievals of fluorescence rely solely upon the filling-in of solar Fraunhofer lines that are not significantly affected by atmospheric absorption. Although these measurements provide near global coverage on a monthly basis, they suffer from relatively low precision and sparse spatial sampling. Here, we describe a new methodology to retrieve global far-red fluorescence information; we use hyperspectral data to disentangle the spectral signatures of three basic components in and surrounding the O₂ A-band: atmospheric absorption, surface reflectance, and fluorescence radiance. Through detailed simulations, we demonstrate the feasibility of the approach and show that moderate spectral resolution measurements with a relatively high signal-to-noise ratio within and outside the O₂ A-band can be used to retrieve far-red fluorescence information with good precision and accuracy. The method is then applied to data from the Global Ozone Monitoring Instrument 2 (GOME-2). The GOME-2 fluorescence retrievals display similar spatial structure as compared with GOSAT. GOME-2 enables global mapping of far-red fluorescence with higher precision over smaller spatial and temporal scales than is possible with GOSAT. It should be noted that both GOME-2 and GOSAT were designed to make atmospheric trace gas measurements and were not optimized for fluorescence measurements. Our approach can be applied to other existing and future space-based instruments that provide moderate spectral resolution observations in the near-infrared region.

O₂ A-band fluorescence retrievals

J. Joiner et al.

Title Page

Abstract

Introduction

Conclusions

References

Tables

Figures



Back

Close

Full Screen / Esc

Printer-friendly Version

Interactive Discussion



1 Introduction

Vegetation releases unused absorbed photosynthetically-active radiation primarily as heat with a small amount re-emitted as fluorescence. Measurements of terrestrial chlorophyll fluorescence are directly related to photosynthetic function and are potentially useful for forest and agricultural applications as well as assessment of the terrestrial carbon budget including gross primary productivity (GPP) (e.g., Lichtenthaler, 1987; Saito et al., 1998; Corp et al., 2003, 2006; Campbell et al., 2008; Damm et al., 2010; Joiner et al., 2011, 2012; Frankenberg et al., 2011b; Guanter et al., 2012). Studies show that in high light conditions, such as in late morning and early afternoon when many satellite measurements are made and when plants are under stress, fluorescence is generally correlated with photosynthesis and light use efficiency (LUE) (e.g., Flexas et al., 2002; Louis et al., 2005; Meroni et al., 2008; Amoros-Lopez et al., 2008; van der Tol et al., 2009; Zarco-Tejada et al., 2009, 2013; Daumard et al., 2010). Fluorescence information is also complementary to reflectance-based spectral vegetation indices (Meroni and Colombo, 2006; Middleton et al., 2008, 2009; Rascher et al., 2009; Meroni et al., 2008; Daumard et al., 2010; Guanter et al., 2007, 2012; Zarco-Tejada et al., 2009, 2013; Joiner et al., 2011, 2012; Frankenberg et al., 2011b); these indices include the Normalized Difference and Enhanced Vegetation Indices (NDVI and EVI, respectively) that are linked to chlorophyll content, and the Photochemical Reflectance Index (PRI) related to changes in xanthophyll cycle pigments (Gamon et al., 1992). In addition, if not accounted for in photon path estimates from the O₂ A-band, fluorescence may propagate errors into retrievals of trace-gas concentrations including CO₂ that require very high accuracy and precision (Frankenberg et al., 2012).

One means of measuring the small fluorescence signal from passive remote sensing instrumentation is to make use of dark features in the Earth's reflected spectrum, either from telluric absorption or deep solar Fraunhofer lines. For example, ground-, aircraft, and space-based approaches have utilized filling-in of the dark and spectrally-wide O₂ A-band (~ 760 nm) and O₂ B-band (~ 690 nm) atmospheric absorption features to

AMTD

6, 3883–3930, 2013

O₂ A-band fluorescence retrievals

J. Joiner et al.

Title Page

Abstract

Introduction

Conclusions

References

Tables

Figures



Back

Close

Full Screen / Esc

Printer-friendly Version

Interactive Discussion



detect the weak fluorescence signal (see e.g., Guanter et al., 2007; Meroni et al., 2009). The spectral location of these oxygen absorption features as well as other absorption bands and solar Fraunhofer lines are shown in Fig. 1 along with the broadband red and far-red fluorescence emission features that peak near 685 and 740 nm, respectively.

Deep solar Fraunhofer lines have also been used to detect fluorescence from vegetation following the early work of e.g. Plascyk and Gabriel (1975). Joiner et al. (2011, 2012), Frankenberg et al. (2011b), and Guanter et al. (2012) used NIR solar Fraunhofer lines, that are filled-in by vegetation fluorescence, to globally map terrestrial fluorescence with the high spectral resolution interferometer aboard the Japanese Greenhouse gases Observing SATellite (GOSAT). Joiner et al. (2012) strongly suggested that fluorescence may also be measurable from space with lower spectral resolution instrumentation as compared with the GOSAT interferometer or similar instruments. They focused on filling-in of the 866 nm Ca II solar Fraunhofer line as measured with the SCanning Imaging Absorption spectroMeter for Atmospheric CHartographyY (SCIAMACHY) satellite instrument. This filling-in appears to be produced by fluorescence from chlorophyll as supported by Gamon and Berry (2013). The SCIAMACHY spectral resolution at this wavelength is about 0.5 nm.

While the current satellite results show promise for use in estimation of GPP, the GOSAT measurements have fairly low spatial sampling and relatively low single-observation precision (Joiner et al., 2011; Frankenberg et al., 2011a; Guanter et al., 2012). The SCIAMACHY results have higher sampling frequency, but the very low signal levels spectrally far from the far-red fluorescence peak also result in low precision for single observations (Joiner et al., 2012). To produce global maps with high enough fidelity for comparisons with other measurements and models, GOSAT and SCIAMACHY fluorescence retrievals must be averaged spatially and/or temporally. In doing so for GOSAT, there is a substantial sampling or representativeness error introduced by the averaging of sparse observations within a relatively large grid box.

Other approaches for satellite fluorescence retrievals have aimed at utilization of the strong atmospheric oxygen bands (A and B bands) that absorb at wavelengths

O₂ A-band fluorescence retrievals

J. Joiner et al.

Title Page

Abstract

Introduction

Conclusions

References

Tables

Figures



Back

Close

Full Screen / Esc

Printer-friendly Version

Interactive Discussion



O₂ A-band fluorescence retrievals

J. Joiner et al.

Title Page

Abstract

Introduction

Conclusions

References

Tables

Figures



Back

Close

Full Screen / Esc

Printer-friendly Version

Interactive Discussion



where chlorophyll fluorescence is emitted. For example, approaches to separate fluorescence features from those of reflectance for space-based measurements have been developed in which atmospheric absorption is assumed to be perfectly modeled (e.g., Mazzoni et al., 2008, 2010, 2012). More complex algorithms have been proposed and tested on simulated data in which the parameters affecting O₂ absorption are retrieved and accounted for using a radiative transfer model (Guanter et al., 2010). Low spectral resolution O₂ A-band satellite measurements from the MEdium Resolution Imaging Spectrometer (MERIS) aboard Envisat have also been used to retrieve information about fluorescence (Guanter et al., 2007). Thus far, these satellite measurements are spatially and temporally limited and require an on-ground non-fluorescing reference target for normalization.

Here, we develop new methodology to retrieve the far-red chlorophyll fluorescence using space-based hyperspectral measurements in and around the O₂ A-band. Instead of exclusively using the filling-in of solar Fraunhofer lines as in the previous works with GOSAT and SCIAMACHY, we demonstrate that fluorescence can be retrieved by exploiting the different spectral structure produced by the far-red chlorophyll fluorescence feature (including both solar and telluric line filling), atmospheric absorption, and surface reflectance. Our approach has an advantage over previous attempts to measure fluorescence from aircraft and space using telluric absorption features in that it does not require a nearby non-fluorescing target.

Our methodology is similar to approaches developed for ground-based instrumentation developed by Guanter et al. (2013) in that radiative transfer in atmospheric absorption bands is approximated statistically using a principal component analysis (PCA) (or singular value decomposition, SVD). SVD approaches have also been applied to satellite fluorescence retrievals using wavelengths not affected by atmospheric absorption (Guanter et al., 2012). In this work, we expand the use of PCA to include the geometry of a space-based instrument for wavelengths where significant atmospheric absorption takes place. This scenario is more complex than for ground-based measurements. Fluorescence emission can be significantly absorbed in the atmosphere. Because this

absorption is different in magnitude from that of reflected sunlight, the scenario for a satellite retrieval is more difficult as compared with that for a ground-based instrument.

We apply our approach to data from the Global Ozone Monitoring Instrument 2 (GOME-2). The primary function of GOME-2 is to make measurements of atmospheric trace gases. While not optimal for fluorescence measurements owing to its relatively large ground footprint and moderate spectral resolution, its high sampling and signal-to-noise ratio enable state-of-the-art fluorescence retrievals in the far-red chlorophyll emission feature. Near-global coverage is provided within a few days.

The paper is organized as follows: Sect. 2 describes the GOME-2 instrument. The details of our retrieval approach are given in Sect. 3.1. Simulations are then conducted to demonstrate its applicability to current and proposed satellite instruments in Sect. 4. Section 5 displays far-red fluorescence maps from GOME-2 and compares them with similar maps derived from GOSAT. We also show changes in retrieved fluorescence and NDVI from GOME-2 over successive ten day segments.

2 GOME-2 satellite data

In this work, we use data from GOME-2. SCIAMACHY provides observations in the same spectral region. While the native SCIAMACHY footprint (30 km × 60 km) is slightly smaller than that of GOME-2 (40 km × 80 km), the spatial sampling of SCIAMACHY is not as good as GOME-2, in part due to alternating between limb and nadir measurements. In addition, SCIAMACHY observations in the near-infrared at some wavelengths were spatially coadded and are not provided at full spatial resolution in the level 1b data set. While we focus on GOME-2 here, our approach can be applied to SCIAMACHY as well.

GOME-2 is an operational nadir-viewing UV/visible cross-track scanning spectrometer (Munro et al., 2006). It flies as part of the European Meteorological Satellite (EU-METSAT) Polar System (EPS) MetOp mission series. GOME-2 measures the Earth's

O₂ A-band fluorescence retrievals

J. Joiner et al.

Title Page

Abstract

Introduction

Conclusions

References

Tables

Figures



Back

Close

Full Screen / Esc

Printer-friendly Version

Interactive Discussion



backscattered radiance and the extraterrestrial solar irradiance at wavelengths between 240 and 790 nm in four detector channels. Here, we use level 1B data from revision R2 in channel 4 that cover wavelengths 590–790 nm with a spectral resolution of approximately 0.5 nm (Callies et al., 2000) and a relatively high SNR (> 1000).

The nadir Earth footprint size is 40 km × 80 km, and the nominal swath width is 1920 km. A single GOME-2 instrument provides global coverage of the Earth’s surface in about 1.5 days. The first flight of GOME-2 is on MetOp-A, launched 19 October 2006 into a polar orbit with an equator crossing local time of 09:30 LT. The second flight, launched 17 September 2012, is also in a morning orbit but 180° out of phase with the first flight model. As such, one or the other instrument is always making measurements on the sunlit part of the Earth, and near global daily coverage is achievable.

3 Retrieval methodology

3.1 General approach

The total reflectance ρ_{tot} , as a function of wavelength λ , measured by a satellite instrument in the NIR spectral region, can be approximated using a Lambertian model with emission from fluorescence, i.e.,

$$\rho_{\text{tot}}(\lambda) = \rho_0(\lambda) + \frac{\rho_s(\lambda)\mathcal{T}(\lambda)\overline{\mathcal{T}}(\lambda)}{1 - \rho_s(\lambda)\overline{\rho}(\lambda)} + \frac{\pi I_F(\lambda)\overline{\mathcal{T}}(\lambda)}{[1 - \rho_s(\lambda)\overline{\rho}(\lambda)]F(\lambda)\cos(\theta_0)}, \quad (1)$$

where $\rho_s(\lambda)$ is the surface reflectance, ρ_0 is the flux reflectance contribution in the absence of surface effects, \mathcal{T} is the total irradiance flux transmittance (including direct and diffuse components), $\overline{\mathcal{T}}$ is the spherical transmittance from the surface to top-of-the-atmosphere (TOA), $\overline{\rho}$ is the spherical reflectance of the atmosphere back to the surface, θ_0 is the solar zenith angle (SZA), $F(\lambda)$ is the observed extraterrestrial solar irradiance, and I_F is the radiance emission from fluorescence at the surface.

O₂ A-band fluorescence retrievals

J. Joiner et al.

Title Page

Abstract

Introduction

Conclusions

References

Tables

Figures

◀

▶

◀

▶

Back

Close

Full Screen / Esc

Printer-friendly Version

Interactive Discussion



In the absence of atmospheric scattering or assuming that the effects of atmospheric scattering are small (i.e., $\rho_0 \approx 0$ and $\rho_s \bar{\rho} \ll 1$), we may rewrite Eq. (1) as

$$\rho_{\text{tot}}(\lambda) = \rho_s(\lambda) \mathcal{T}(\lambda) \overline{\mathcal{T}}(\lambda) + \frac{\pi I_F(\lambda) \overline{\mathcal{T}}(\lambda)}{F(\lambda) \cos(\theta_0)}, \quad (2)$$

where $\mathcal{T}(\lambda)$ and $\overline{\mathcal{T}}(\lambda)$ now include atmospheric molecular absorption only. We now combine \mathcal{T} and $\overline{\mathcal{T}}$ into a single parameter $\mathcal{T}_2(\lambda) = \mathcal{T}(\lambda) \overline{\mathcal{T}}(\lambda)$ that represents the sun to satellite (2-way) atmospheric transmittance. Using

$$\begin{aligned} \mathcal{T}_2(\lambda) &= \exp[-A_2(\lambda)] \\ &= \exp[-A_v(\lambda) \{ \sec(\theta) + \sec(\theta_0) \}], \end{aligned} \quad (3)$$

where θ is the satellite view zenith angle (VZA), and A_2 and A_v represent the 2-way and vertical absorptances, respectively, and the upwards absorptance, \overline{A} , as

$$\begin{aligned} \overline{A}(\lambda) &= A_v(\lambda) \sec(\theta) \\ &= A_2(\lambda) \frac{\sec(\theta)}{\sec(\theta) + \sec(\theta_0)}, \end{aligned} \quad (4)$$

then

$$\overline{\mathcal{T}}(\lambda) = \exp \left(\ln[\mathcal{T}_2(\lambda)] \frac{\sec(\theta)}{\sec(\theta) + \sec(\theta_0)} \right). \quad (5)$$

Note that the above equations are strictly valid only for monochromatic radiation.

The basic idea behind our approach is to separate the spectral features related to three basic components: atmospheric absorption and scattering, surface reflectivity (ρ_s), and fluorescence radiance (I_F). Note that ρ_0 , $\bar{\rho}$, $\overline{\mathcal{T}}$, and \mathcal{T} , in the presence of atmospheric scattering and in the absence of atmospheric molecular absorption, are

**O₂ A-band
fluorescence
retrievals**

J. Joiner et al.

Title Page

Abstract

Introduction

Conclusions

References

Tables

Figures

◀

▶

◀

▶

Back

Close

Full Screen / Esc

Printer-friendly Version

Interactive Discussion



O₂ A-band fluorescence retrievals

J. Joiner et al.

Title Page

Abstract

Introduction

Conclusions

References

Tables

Figures

◀

▶

◀

▶

Back

Close

Full Screen / Esc

Printer-friendly Version

Interactive Discussion



a spectrally smooth function of wavelength. Therefore, when atmospheric scattering is present, $\rho_s(\lambda)$ and $I_F(\lambda)$ in Eq. (2) can be thought of as effective TOA spectral components of surface reflectance and fluorescence that have been modified by spectrally smooth atmospheric scattering; the spectral structure of ρ_0 can be incorporated into the components of the first term of Eq. (2).

To solve for ρ_s , I_F , and \mathcal{T}_2 , we assume that each has a distinct spectral structure. We represent the fluorescence far-red emission, $I_F(\lambda)$, as a Gaussian function of λ centered at 736.8 nm with full-width at half-maximum (FWHM) value of 21.2 nm similar to Subhash and Mohanan (1997) and Zarco-Tejada et al. (2000). We further assume that $\rho_s(\lambda)$, within our limited spectral fitting window, is spectrally smooth and model it as a low order polynomial in λ . Alternative parameterizations for fluorescence and reflectance have been explored (e.g., Mazzoni et al., 2010, 2012). Previous works suggest that small errors in the prescribed shape of the fluorescence emission have little impact on the estimated peak fluorescence value (Daumard et al., 2010; Fournier et al., 2012; Guanter et al., 2013). We estimate the spectral structure of \mathcal{A}_2 (or \mathcal{T}_2) using principal components (PCs) as described below.

In principle, our approach may be applied to the entire fluorescence emission band shown in Fig. 1 containing both the red and far-red features. Alternatively, different fitting windows could be used to estimate fluorescence within smaller wavelength ranges. As a starting point to demonstrate our approach, we focus on retrievals of the far-red fluorescence that fills in the O₂ A-band.

It is difficult to accurately estimate retrieval errors with our approach using standard linear techniques. Firstly, because our inverse problem is non-linear, typical linear methods of estimating errors may not be applicable. Secondly, our approach relies on an empirical rather than a physical approach for deriving atmospheric absorption; this makes it difficult to quantify forward model errors.

3.2 Simulated radiances and irradiances

To quantify retrieval errors, we conduct detailed simulations over a wide range of conditions. We also use simulated data to assess the impact of instrument specifications including the signal-to-noise ratio (SNR) and spectral resolution on fluorescence retrievals. Finally, we test different retrieval scenarios, such as various spectral fitting windows and numbers of retrieved parameters, using the simulated radiances.

We simulate top-of-the-atmosphere (TOA) sun-normalized radiances using the Matrix Operator Model (MOMO) radiative transfer model (Fell and Fischer, 2001; Preusker and Lindstrot, 2009). The radiance calculations utilize absorption line strengths and widths from the high-resolution atmospheric radiance and transmittance model code (HITRAN) 2008 dataset (Rothman et al., 2009). The radiances are computed monochromatically and are sampled at 0.005 nm. They are then multiplied by a solar spectrum sampled in the same way and finally convolved with various instrument line shape functions.

We use solar data originally sampled at 0.001 nm from kurucz.harvard.edu/sun/irradiance2005/irradthu.dat similar to Chance and Kurucz (2010) but more highly sampled. Figure 2 shows simulated solar spectra generated for different instrument specifications including a spectral resolution similar to SCIAMACHY and GOME-2 (FWHM = 0.5 nm sampled at 0.2 nm) and a smaller FWHM of 0.3 nm sampled at 0.1 nm. Significant solar Fraunhofer line structure can be seen throughout the spectrum with deeper structures at the higher spectral resolution.

Note that we do not simulate the effects of rotational-Raman scattering (RRS) or O₂ A-band dayglow emissions. RRS effects are generally small, though not negligible, at the wavelengths of interest (Vasilkov et al., 2012). The effects of O₂ A dayglow emissions in the upper atmosphere are also expected to be small (Guanter et al., 2010). Directional effects of the vegetation reflectance and fluorescence are also not simulated.

O₂ A-band fluorescence retrievals

J. Joiner et al.

Title Page

Abstract

Introduction

Conclusions

References

Tables

Figures



Back

Close

Full Screen / Esc

Printer-friendly Version

Interactive Discussion



O₂ A-band fluorescence retrievals

J. Joiner et al.

Title Page

Abstract

Introduction

Conclusions

References

Tables

Figures



Back

Close

Full Screen / Esc

Printer-friendly Version

Interactive Discussion



Radiances are computed for two view zenith angles ($VZA = 0^\circ$ and 16°), four solar zenith angles ($SZA = 15^\circ, 30^\circ, 45^\circ, 70^\circ$), two atmospheric temperature profiles (middle latitude summer and winter), four surface pressures (955, 980, 1005, and 1030 hPa), four values of total column water vapor (0.5, 1.5, 2.5, and 4.0 cm), five aerosol optical thicknesses at 550 nm (0.05, 0.12, 0.2, 0.3, and 0.4), and three aerosol plume heights (700–900, 600–800, and 500–700 hPa) with a continental aerosol model. Two separate data sets are created, one without fluorescence intended for principal component analyses (henceforth referred to as “training”), and one containing fluorescence intended to examine retrieval performance with the simulated radiances (referred to as “testing”). The training data set uses a spectral library of ten different surface reflectance spectra corresponding to soil and snow. This provides a total of 38400 samples in the training data set.

The testing data set contains surface reflectance and fluorescence emission spectra generated with the FluorSAIL and FluorMODleaf codes (Jacquemoud et al., 2009; Pedrós et al., 2010; Miller et al., 2005). A given input leaf-level fluorescence spectrum has been scaled by multiplicative factors. Different values of chlorophyll content (from 5 to $40 \mu\text{g cm}^{-2}$) and leaf area index (from 0.5 to 4) have been used for the propagation of the resulting leaf-level fluorescence spectra to the canopy level. There are sixty distinct top-of-canopy fluorescence spectra from these combinations as shown in Fig. 3. Top-of-canopy reflectance spectra are consistently generated by the leaf and canopy codes for the same combinations of chlorophyll content and leaf area index. Other parameters in the models were set to default values as in Guanter et al. (2010). This gives a total of 230 400 different samples in the testing data set.

3.3 Generation of atmospheric PCs

Radiative transfer in the O₂ A-band is complex because the depth of the absorption features depends upon the surface pressure and albedo as well as the vertical structure of atmospheric temperature and cloud/aerosol particles (e.g., Preusker and Lindstrot, 2009). Retrieval algorithms have been developed to retrieve some or all of

these parameters using O₂ A-band radiances (e.g., Guanter et al., 2007; O'Dell et al., 2012). Other factors such as filling-in from rotational-Raman scattering are typically not accounted for and will therefore further complicate such algorithms (Vasilkov et al., 2012). Instrumental effects such as non-linearity also challenge physically-based approaches used to estimated O₂ A-band absorption.

Instead of using radiative transfer calculations, we have developed an empirically-based alternative for estimation of A_2 or $\mathcal{T}_2(\lambda)$; we represent $A_2(\lambda)$ as a linear combination of principal components (PCs) $\phi_j(\lambda)$ that can be estimated using simulated or real satellite data, i.e.,

$$A_2(\lambda) = \sum_{i=1}^n a_i \phi_i(\lambda), \quad (6)$$

where a_i are the coefficients of the PCs. Instead of using laboratory-measured absorption cross-sections as is typical in the differential optical absorption spectroscopy (DOAS) approach, we use atmospheric spectra, simulated or measured, to derive the spectral components of absorption.

As in the DOAS approach, our method implicitly assumes that the Beer–Lambert law of weak linear absorption applies, although the PCs may be able to incorporate some features of non-linear absorption. Because this law does not strictly apply to the O₂ A-band where individual lines may become optically thick and absorption is temperature dependent, simulations are needed to verify the applicability of the above equations. To the extent that this is successful, there are several advantages of our approach. By using PCs, we do not need to estimate parameters affecting O₂ and H₂O absorption such as surface pressure, temperature and water vapor profiles, and cloud and aerosol parameters that affect nearly all satellite observations. In addition, we eliminate dependence upon a precise specification of the instrument response function. The PCs may also capture instrument artifacts as well as the effects of RRS that are otherwise difficult to quantify.

O₂ A-band fluorescence retrievals

J. Joiner et al.

[Title Page](#)[Abstract](#)[Introduction](#)[Conclusions](#)[References](#)[Tables](#)[Figures](#)[⏪](#)[⏩](#)[◀](#)[▶](#)[Back](#)[Close](#)[Full Screen / Esc](#)[Printer-friendly Version](#)[Interactive Discussion](#)

O₂ A-band fluorescence retrievals

J. Joiner et al.

Title Page

Abstract

Introduction

Conclusions

References

Tables

Figures

◀

▶

◀

▶

Back

Close

Full Screen / Esc

Printer-friendly Version

Interactive Discussion



As in DOAS retrievals, we use the logarithm of sun-normalized radiance spectra for the PCA. We first compute PCs with the simulation training data set. For comparison, we also generate PCs using actual GOME-2 satellite radiance data. For the GOME-2 PCA, we use spectra from a single day (1 May 2007) consisting of observations over sea ice, snow/ice-covered land, the Sahara desert, and cloudy ocean for pixels with $\theta_o < 85^\circ$. For the cloudy ocean data, we compute the reflectance at 670 nm (ρ_{670}) and use observations only for $\rho_{670} > 0.7$.

For both real and simulated data, we normalize the spectra with respect to a second order polynomial fit to wavelengths not significantly affected by atmospheric absorption (i.e., 712–713 nm, 748–757 nm, and wavelengths > 775 nm) before taking the logarithm of the spectra. This normalization produces values representative of the total sun to satellite absorptance. Alternatively, PCAs may be similarly performed without taking the logarithm of the normalized spectra in order to model transmittance instead of absorptance.

Absorption affecting fluorescence in the far-red emission feature includes that from the O₂ A-band near 760 nm as well as a weaker water vapor band at shorter wavelengths. Figure 4 shows examples of normalized spectra approximating the sun-to-satellite transmittance separately for two wavelength ranges: (1) 712–747 nm, dominated by H₂O absorption, and (2) 747–783 nm encompassing the O₂ A-band.

Figure 5 shows the leading four PCs for the wavelength range 712–747 nm computed with simulated data for FWHMs of 0.5 nm (similar to GOME-2) and 0.3 nm. The spectral variance in this window is due almost exclusively to water vapor absorption. The variance explained (with respect to the total) as well as the cumulative variances explained are indicated. The PCs are similar for the two spectral resolutions with somewhat deeper structures at the higher resolution. The variance explained by the leading PCs is similar for the two spectral resolutions.

Figure 6 similarly shows PCs generated from actual GOME-2 satellite data. PCs and variance explained are similar for the simulated and GOME-2 data. However, PC #4 from GOME-2 appears to correspond to PC #3 from the simulated data, and there is no

similar correspondence between PC #3 from GOME-2 and PC #4 from the simulation. The first PC explains over 99 % of the spectral variance and 99.99 % of the variance is captured in the first four modes for both the simulated and GOME-2 data.

Figures 7 and 8 similarly show the leading PCs for the spectral window 747–783 nm dominated by strong oxygen A-band absorption near 760 nm. Again, the PCs are similar for simulated and GOME-2 satellite data with over 99.9 % of variance captured by the leading mode and more than 99.999 % of the variance explained by the first four modes. PCs #2 and #3 appear to be reversed for the GOME-2 and simulated data.

3.4 Solving the non-linear problem

To solve the non-linear estimation problem, we use a gradient-expansion algorithm adapted from Marquardt (1963) and Bevington (1969). This algorithm provides a relatively fast convergence, typically 4–6 iterations. We derive and supply to this algorithm the analytic Jacobians or partial derivatives of the observed radiances with respect to the state variables.

Typical Jacobians (i.e., partial derivatives of the reflectances with respect to the coefficients of the PCs, reflectance polynomials, and the peak value of the far-red fluorescence feature at 736.8 nm) are shown in Fig. 9 for FWHMs of 0.5 and 0.3 nm. Although the components are not completely orthogonal, our simulation results will show that fluorescence can be successfully disentangled from atmospheric and surface parameters. Subtle differences in the Jacobians enable this differentiation. For example, small Fraunhofer structures can be seen in the fluorescence Jacobian at wavelengths between about 745 and 758 nm that are not seen in the other Jacobians. An instrument with a high enough spectral resolution and SNR should be able to detect these features as will be demonstrated below. Again, deeper spectral structures are seen at the higher spectral resolution.

At convergence, the partial derivatives contained in the Jacobian \mathbf{K} matrix may be used to examine potential error correlations through an unconstrained linear error estimation, i.e.,

O₂ A-band fluorescence retrievals

J. Joiner et al.

Title Page

Abstract

Introduction

Conclusions

References

Tables

Figures



Back

Close

Full Screen / Esc

Printer-friendly Version

Interactive Discussion



$$\mathbf{E} = (\mathbf{K}^T \mathbf{S}_e^{-1} \mathbf{K})^{-1}, \quad (7)$$

where \mathbf{E} is the retrieval error covariance matrix, and \mathbf{S}_e is the measurement error covariance. For example, if we assume random and uncorrelated wavelength-independent radiance errors with a fitting window between 747 and 783 nm and a state vector containing the peak value of the fluorescence far-red feature defined by a Gaussian spectral shape, coefficients for 25 PCs, and a 3rd order polynomial to represent $R(\lambda)$, we find that the computed errors for the far-red fluorescence peak are moderately correlated with the constant reflectivity term and some of the leading PCs.

3.5 Processing of GOME-2 data

3.5.1 GOME-2 fluorescence retrievals

We use a fitting window from 712–783 nm for GOME-2 retrievals with a fourth order polynomial to model the surface reflectivity and a Gaussian function for the canopy-level far-red fluorescence as described above. We used 25 PCs for each of the two PCA subwindows shown above. A PCA is conducted daily for each sub-window as described above using the daily-measured solar flux. No adjustments are made to the calibrated radiances/irradiances; it should be noted that the MetOp-A GOME-2 is known to have suffered from radiometric degradation over its lifetime.

3.5.2 Cloud filtering and quality control

As in Joiner et al. (2012), we compute the effective cloud fraction f_c and eliminate data with $f_c > 0.4$. To compute f_c , we use the black-sky 16 day gridded filled-land surface albedo product from Aqua MODIS (MOD43B3) at 656 nm (Lucht et al., 2000). Application of more or less stringent limits on cloud contamination within a moderate range did not substantially alter the derived spatial and temporal patterns of I_F .

O₂ A-band fluorescence retrievals

J. Joiner et al.

Title Page

Abstract

Introduction

Conclusions

References

Tables

Figures



Back

Close

Full Screen / Esc

Printer-friendly Version

Interactive Discussion



For the remainder of this section, all retrievals will use 25 PCs for each of the two sub-windows.

4.2 Sensitivity to signal-to-noise ratio

For comparison, Table 1 shows results of fluorescence retrievals using simulated observations as above with SNR = 1000. Results may be compared with the 25 PC case (line 4) described in Sect. 4.1 for an instrument with SNR = 2000. Standard deviations and root-mean-squared (RMS) errors for SNR = 1000 are slightly less than twice those at SNR = 2000. This is consistent with the expected behavior of a retrieval based solely on solar Fraunhofer line structure, where errors are inversely proportional to SNR with all other parameters held constant (Joiner et al., 2012).

4.3 Sensitivity to the fitting window

In the experiments shown in lines 6–10 of Table 1, we use different fitting windows for an instrument with SNR = 2000 and FWHM = 0.5 nm. Fluorescence errors are approximately a factor of two smaller with the 712–747 nm fitting window as compared with the 747–780 nm shown above. This demonstrates that fluorescence retrievals can be obtained with good precision without using the filling-in signal from the O₂ A-band. The 712–747 nm window spans the peak far-red fluorescence and also contains H₂O absorption. A reduced fitting window of 723–747 nm produces slightly degraded results as compared with the 712–747 nm window. Both of these shorter-wavelength windows show decreased bias as compared with the 747–780 nm window that includes the O₂ A-band. Our results are consistent with those of Guanter et al. (2013) who similarly showed that fitting windows in this spectral region, without the benefit of the O₂ A-band, can be used to retrieve fluorescence with higher spectral resolution ground-based instruments.

Table 1 also examines results for fitting windows more confined to the O₂ A-band. As may be expected, retrievals are degraded for a smaller fitting window of 755–775 nm

O₂ A-band fluorescence retrievals

J. Joiner et al.

Title Page

Abstract

Introduction

Conclusions

References

Tables

Figures



Back

Close

Full Screen / Esc

Printer-friendly Version

Interactive Discussion



O₂ A-band fluorescence retrievals

J. Joiner et al.

Title Page

Abstract

Introduction

Conclusions

References

Tables

Figures

◀

▶

◀

▶

Back

Close

Full Screen / Esc

Printer-friendly Version

Interactive Discussion



as compared with the 747–780 nm window used above. Results are also shown with a smaller fitting window of 759–768 nm. This window consists primarily of the O₂ A-band with embedded Fraunhofer structure. Note that the strongest solar Fraunhofer feature within the range 712–783 nm occurs inside the O₂ A-band region near 766 nm. Results are significantly degraded with this limited fitting window. Frankenberg et al. (2011a) noted the difficulties associated with disentangling fluorescence spectral information from that of aerosols, clouds, surface pressure, etc., using only wavelengths within O₂ A-band spectral region. Although there is a significant correlation between fluorescence and these other parameters, there is never-the-less a limited ability to retrieve information about fluorescence within this absorption band. However, biases increase as the fitting window is more confined to the O₂ A-band spectral region. Precision is significantly degraded with a limited fitting window of 747–758 nm containing only weak solar Fraunhofer line structures, while the accuracy for this fitting window is good.

4.4 Sensitivity to spectral resolution

Lines 12–13 of Table 1 show retrieval statistics for an instrument with FWHM = 0.3 nm, sampling of 0.1 nm, and SNR of 2000 for fitting windows of 747–780 nm and 712–747 nm, respectively. The precision is significantly improved as compared with FWHM = 0.5 nm retrievals. We also varied the fitting window as in Sect. 4.3 for FWHM = 0.3 nm and reached the same conclusions as with FWHM = 0.5 nm.

As described above, there are 60 distinct values of fluorescence (averaged between 740 and 780 nm) ranging from near zero to near 4 mWm⁻² nm⁻¹ sr⁻¹. For each value, the observing conditions vary (e.g., different SZAs, VZAs, surface pressures, temperature profiles, and aerosol parameters). Figure 11 shows retrieval results using the 712–747 nm fitting window for the FWHM = 0.3 and 0.5 nm simulated data. This figure shows that biases are more prevalent for higher levels of fluorescence. This was the case for the simulations with the larger fitting windows.

4.5 Radiance residuals from simulated data

Figure 12 shows RMS of the radiance residuals (observed minus calculated radiance) for two cases with FWHM = 0.3 nm, SNR = 2000, and a fitting window of 747–780 nm: (1) fluorescence is not retrieved and (2) fluorescence is retrieved. The RMS of the residual is computed at each wavelength averaged over all conditions in the simulation testing data and shown as a percentage of observed radiance. As expected, reductions in the residuals are achieved when fluorescence is retrieved, particularly in the vicinity of deep solar Fraunhofer lines (e.g., near 749, 751, and 766 nm). These improvements occur throughout the full spectral range. Note that relatively larger residuals are produced at the the low radiance levels found within the deep O₂ A-band.

5 Results from GOME-2 data

5.1 Radiance residuals from GOME-2

Figure 13 shows the spectral RMS of the radiance residuals over the GOME-2 fitting window for a single day. Residuals are averaged for each wavelength over all observations with SZA < 70° and NDVI > 0.3 (i.e., moderately to highly vegetated pixels) that passed quality control and cloud filtering checks. Reductions in the residuals can be seen throughout the spectral range with a similar spectral structure as shown in Fig. 12 for the simulated data (i.e., reductions at the deep solar Fraunhofer lines). Some reduction is also seen at the deepest part of the O₂ A-band near 760 nm. In the portions of the fitting window that are relatively free of atmospheric absorption, the residuals are consistent with a GOME-2 SNR of 1000 or greater. Residuals have similar magnitudes to those shown in Fig. 12 for simulated data with SNR = 2000. Residuals are somewhat higher in regions where atmospheric absorption is present such as in the water vapor absorption band shortward of about 747 nm.

Title Page

Abstract

Introduction

Conclusions

References

Tables

Figures

⏪

⏩

◀

▶

Back

Close

Full Screen / Esc

Printer-friendly Version

Interactive Discussion



5.2 Comparison of GOME-2 and GOSAT fluorescence

Global composites of I_F referenced to 737 nm derived from GOME-2 for July, December and the annual average in 2009 are displayed in Fig. 14. For comparison, maps of I_F at 757 nm from GOSAT-FTS retrievals are also shown for the same time periods (the annual average is from June 2009 through May 2010 for GOSAT). The GOSAT-FTS retrievals were performed and processed with the algorithm described in Guanter et al. (2012). Quality-filtered GOME-2 retrievals have been averaged in 0.5° latitude-longitude grid boxes, whereas a 2° grid is used for the GOSAT retrievals that have a much more sparse spatial sampling than GOME-2.

A very good agreement of the I_F spatial patterns is observed between the two data sets, although improvements in spatial resolution and precision are obvious in the GOME-2 maps. High I_F values are observed over densely vegetated areas. Globally, the highest I_F signal is found in July in the Eastern United States. High I_F values are also observed in some parts of South America and Africa in December. I_F values near zero are detected in July over Greenland (zero to slightly negative), in December over Antarctica (zero to slightly positive), and during the entire year over the Sahara desert and most of Australia. These spatial patterns compare well with those observed in the I_F maps derived from GOSAT-FTS for the same time periods. The overall excellent spatial agreement between GOME-2 and GOSAT can be considered as a validation of our GOME-2 I_F retrievals, given the fact that the GOME-2 retrieval approach is much more complicated and prone to systematic errors as compared with that of GOSAT.

Concerning the annual averages of I_F retrievals, the main difference between the two data sets is in the tropical rainforest, especially in Africa and Indonesia. GOME-2 I_F is in relative terms significantly lower than GOSAT's over those areas. This may be due to a larger impact of cloud contamination in coarser GOME-2 footprint data ($40 \text{ km} \times 80 \text{ km}$ for GOME-2 as compared with around a 10 km diameter for GOSAT). The different solar illumination angles encountered by the two instruments may also

O₂ A-band fluorescence retrievals

J. Joiner et al.

Title Page

Abstract

Introduction

Conclusions

References

Tables

Figures



Back

Close

Full Screen / Esc

Printer-friendly Version

Interactive Discussion



contribute to relative differences between high and low latitudes as described in more detail below.

Peak I_F values derived from GOSAT are around $1.8 \text{ mWm}^{-2} \text{ sr}^{-1} \text{ nm}^{-1}$ at 757 nm. This is about 50% lower than the peak values for GOME-2, and roughly consistent with the expected differences owing to the different reference retrieval wavelengths in each case (737 and 757 nm for GOME-2 and GOSAT, respectively). However, the overpass times of the satellites also plays a role ($\sim 09:30$ LT for MetOp-A, $\sim 13:00$ LT for GOSAT). GOME-2 measurements have systematically higher solar zenith angles (SZAs) as compared with GOSAT. In general, the illumination angle affects the fluorescence signal at the top-of-canopy through (1) the intensity of the sunlight incident at the canopy (2) the amount of illuminated leaves that is related to the ratio of of diffuse-to-direct irradiance, and (3) the physiological relationship between photosynthesis, fluorescence, and heat dissipation. The analysis of the effects of the illumination angle on the I_F signal will be explored in future works.

The standard deviation of the July and December I_F retrievals in Fig. 15a, b indicate the variability of the I_F values observed in each $0.5^\circ \times 0.5^\circ$ gridbox. Causes for this variability are instrumental noise, natural variability in vegetation activity within the month, residual cloud effects, and the different footprints from various MetOp-A orbits. It can be seen that the highest variability in the retrievals is found over a large area in South America, and that this does not depend on the season. Instrument performance in this region is substantially degraded by the SAA. Even though this effect does not appear to have a large impact on the monthly average in Fig. 14a and b, the data over this area must be handled carefully. Concerning the rest of the globe, the standard deviation patterns compare well with the expected at-sensor radiance patterns (e.g., higher standard deviations over bright snow-covered areas and deserts) that can be explained by the higher contribution of photon noise triggered by higher at-sensor radiance levels.

Figure 15c, d shows the number of I_F retrievals fulfilling the quality criteria per gridbox. Typically, 10–20 retrievals are available for each grid box within a month. Those numbers are smaller over highly cloudy tropical rainforest regions, especially during

O₂ A-band fluorescence retrievals

J. Joiner et al.

Title Page

Abstract

Introduction

Conclusions

References

Tables

Figures

◀

▶

◀

▶

Back

Close

Full Screen / Esc

Printer-friendly Version

Interactive Discussion



the wet season in December, and at high latitudes. Note that the red orbital stripes are not artifacts, but are due to narrow swath data that are obtained approximately once per month.

5.3 Temporal variations in GOME-2 fluorescence and NDVI

The high revisit time of GOME-2 allows for excellent temporal sampling in the derived vegetation products. This is illustrated in Fig. 16. The figure shows 10 day composites of I_F and NDVI derived from GOME-2 data between day-of-year (DOY) 131 (11 May) and 160 (10 June) of 2009. Here, fluorescence values are normalized by the cosine of the solar zenith angle in order to minimize the latitudinal and temporal variations in fluorescence owing to the incoming PAR. A lower signal-to-noise ratio is observed for these 10 day composites with respect to the monthly averages in Fig. 14, especially in the area in South America region affected by the SSA. Spatial gaps in the data are due to persistent cloud contamination, as MetOp provides near-daily global coverage.

We use a standard definition to compute NDVI from GOME-2, i.e.,

$$\text{NDVI} = \frac{\rho_{\text{NIR}} - \rho_{\text{RED}}}{\rho_{\text{NIR}} + \rho_{\text{RED}}}, \quad (8)$$

where the ρ_{NIR} and ρ_{RED} are computed using single wavelength observations closest to 780 and 670 nm, respectively. Note that the values of ρ_{NIR} and ρ_{RED} have not been corrected for atmospheric scattering, surface BRDF effects, or fluorescence and are affected by cloud contamination within the GOME-2 footprint. Despite the simplicity of the GOME-2 NDVI calculation, spatial patterns are similar to those of the MODIS NDVI product (not shown). The GOME-2 NDVI sampling is identical to that of the GOME-2 fluorescence.

Phenological changes in the Northern Hemisphere are clearly visible from one 10 day period to another in Fig. 16. A strong increase in I_F is observed in Europe from DOYs 131–140 to DOYs 141–150. This rapid change in green biomass is also detectable in the NDVI, although with a smaller intensity. This high temporal sampling of

O₂ A-band fluorescence retrievals

J. Joiner et al.

Title Page

Abstract

Introduction

Conclusions

References

Tables

Figures



Back

Close

Full Screen / Esc

Printer-friendly Version

Interactive Discussion



I_F trends cannot be achieved with GOSAT data owing to the significantly lower number of observations and the sparse spatial sampling. Improved temporal sampling should be achievable by processing data from both GOME-2 instruments for the periods of dual measurements.

6 Conclusions

We have developed a new approach to retrieve far-red fluorescence from moderate spectral resolution satellite instruments. The method utilizes fluorescence filling-in of the O_2 A and water vapor bands as well as the surrounding weak solar Fraunhofer lines; it relies upon the separation of spectral signatures produced by upwelling chlorophyll fluorescence and atmospheric absorption as well as surface, cloud, and aerosol backscattering of solar radiation. We use principal components, derived from data free of fluorescence, to estimate the spectral structure of atmospheric absorption. This information is incorporated into a simplified radiative transfer model that accounts for atmospheric absorption of fluorescence emissions. Through detailed simulations, we show that high quality fluorescence retrievals can be obtained using instrumentation with high SNR and moderate spectral resolution similar to GOME-2 and SCIAMACHY. Retrieval errors depend upon the instrument SNR, spectral resolution, and specification of the spectral fitting window.

We then applied our new approach to satellite moderate spectral resolution measurements from GOME-2. The GOME-2 retrievals compare well with those from GOSAT that are processed with a less complex algorithm, providing further confidence in our approach and implementation with real data. Owing to the excellent spatial sampling and high signal-to-noise ratio of the GOME-2 measurements, we are able to map far-red terrestrial fluorescence at higher spatio-temporal resolutions than previously published GOSAT and SCIAMACHY data. This mapping shows clearly for the first time a northward shift in PAR-normalized fluorescence within a single month as the sun shifts northward during the boreal spring.

O₂ A-band fluorescence retrievals

J. Joiner et al.

Title Page

Abstract

Introduction

Conclusions

References

Tables

Figures

◀

▶

◀

▶

Back

Close

Full Screen / Esc

Printer-friendly Version

Interactive Discussion



O₂ A-band fluorescence retrievals

J. Joiner et al.

Title Page

Abstract

Introduction

Conclusions

References

Tables

Figures

◀

▶

◀

▶

Back

Close

Full Screen / Esc

Printer-friendly Version

Interactive Discussion



Several satellite instruments with NIR spectral coverage and various spectral and spatial resolutions have flown, are currently flying, or are planned for launch in the next few years. The approach outlined here can potentially be applied to these instruments. In addition to GOME-2 and SCIAMACHY, these instruments include GOSAT, the Orbiting Carbon Observatory-2 (OCO-2) (Crisp et al., 2004), planned for launch in 2014, and the TROPospheric Monitoring Instrument (TROPOMI) (Veeffkind et al., 2012) to launch in 2015. The FLuorescence EXplorer (FLEX) (Rascher, 2007; European Space Agency, 2008), an ESA Explorer 8 Mission, selected for Phase A/B1 in early 2011, plans to utilize the O₂ A- and B-bands for chlorophyll fluorescence retrievals (Guanter et al., 2010) and other bio-spectral information across the visible-NIR spectrum. FLEX would provide measurements at a higher spatial resolution than current satellite sensors that were not designed for fluorescence measurements.

Acknowledgements. Funding for this work was provided by the NASA Carbon Cycle Science program (NNH10DA001N) managed by Diane E. Wickland and Richard Eckman and by the Emmy Noether Programme (GlobFluo project) of the German Research Foundation. The authors are indebted to Phil Durbin and his team for assistance with the satellite data sets, particularly the GOME-2 data. We gratefully acknowledge the European Meteorological Satellite (EUMetSat) program, the GOSAT project, and the MODIS data processing team for making available the GOME-2, GOSAT, and MODIS data, respectively, used here. We also thank William Cook, Yen-Ben Cheng, Qingyuan Zhang, Jianping Mao, Rose Munro, Rüdiger Lang, Petya Campbell, Lawrence Corp, Wouter Verhoef, and Arlindo da Silva for helpful discussions. This work was enabled by collaborations forged at the fluorescence workshop held at the California Institute of Technology Keck Institute for Space Studies, funded by the W. M. Keck Foundation. We gratefully acknowledge the organizers of this workshop including Joseph Berry, Paul Wennberg, and Michele Judd.

References

- Amoros-Lopez, J., Gomez-Chova, L., Vila-Frances, J., Alonso, L., Calpe, J., Moreno, J., and del Valle-Tascon, S.: Evaluation of remote sensing of vegetation fluorescence by the analysis of diurnal cycles, *Int. J. Remote Sens.*, 29, 5423–5436, 2008. 3885
- 5 Bevington, P. R.: Data reduction and error analysis for the physical sciences, McGraw Hill, 1969. 3896
- Campbell, P. K. E., Middleton, E. M., Corp, L. A., and Kim, M. S.: Contribution of chlorophyll fluorescence to the apparent vegetation reflectance, *Sci. Total Environ.*, 404, 433–439, 2008. 3885
- 10 Chance, K. and Kurucz, R. L.: An improved high-resolution solar reference spectrum for Earth's atmosphere measurements in the ultraviolet, visible, and near infrared, *J. Quant. Spectrosc. Ra.*, 111, 1289–1295, 2010. 3892, 3916
- Corp, L. A., McMurtrey, J. E., Middleton, E. M., Mulchi, C. L., Chappelle, E. W., and Daughtry, C. S. T.: Fluorescence sensing systems: in vivo detection of biophysical variations in field corn due to nitrogen supply, *Remote Sens. Environ.*, 86, 470–479, 2003. 3885
- 15 Corp, L. A., Middleton, E. M., McMurtrey, J. E., Campbell, P. K. E., and Butcher, L. M.: Fluorescence sensing techniques for vegetation assessment, *Appl. Optics*, 45, 1023–1033, 2006. 3885
- 20 Callies, C., Corpaccioli, E., Eisinger, M., Hahne, A., and Lefebvre, A.: GOME-2 – MetOp's Second-Generation Sensor for Operational Ozone Monitoring, available at: <http://esamultimedia.esa.int/docs/metop/GOME-2-102.pdf> (last access: 13 April 2013), *ESA Bull.-Eur. Space*, 103, 28–36, 2000. 3889
- Crisp, D., Atlas, R. M., Breon, F.-M., Brown, L. R., Burrows, J. P., Ciaï, P., Connor, B. J., Doney, S. C., Fung, I. Y., Jacob, D. J., Miller, C. E., O'Brien, D., Pawson, S., Randerson, J. T., Rayner, P., Salawitch, R. J., Sander, S. P., Sen, B., Stephens, G. L., Tans, P. P., Toon, G. C., Wennberg, P. O., Wofsy, S. C., Yung, Y. L., Kuang, Z., Chudasama, B., Sprague, G., Weiss, B., Pollock, R., Kenyon, D., and Schroll, S.: The Orbiting Carbon Observatory (OCO) mission, *Adv. Space Res.*, 34, 700–709, 2004. 3906
- 25 Damm, A., Elbers, J., Erler, A., Gioli, B., Hamdi, K., Hutjes, R. W. A., Kosvancova, M., Meroni, M., Miglietta, F., Moersch, A., Moreno, J., Schickling, A., Sonnenschein, R., Udelhoven, T., Van Der Linden, S., Hostert, P., and Rascher, U.: Remote sensing of sun-induced
- 30

AMTD

6, 3883–3930, 2013

O₂ A-band fluorescence retrievals

J. Joiner et al.

Title Page

Abstract

Introduction

Conclusions

References

Tables

Figures

◀

▶

◀

▶

Back

Close

Full Screen / Esc

Printer-friendly Version

Interactive Discussion



O₂ A-band fluorescence retrievals

J. Joiner et al.

Title Page

Abstract

Introduction

Conclusions

References

Tables

Figures

◀

▶

◀

▶

Back

Close

Full Screen / Esc

Printer-friendly Version

Interactive Discussion



fluorescence to improve modeling of diurnal courses of gross primary production (GPP),
Glob. Change Biol., 16, 171–186, 2010. 3885

Daumard, F., Champagne, S., Fournier, A., Goulas, Y., Ounis, A., Hanocq, J.-F., and Moya, I.:
A field platform for continuous measurement of canopy fluorescence, IEEE T. Geosci. Re-
5 mote., 48, 3358–3368, 2010. 3885, 3891

European Space Agency: ESA SP-1313/4 Candidate Earth Explorer Core Mis-
sions – Reports for Assessment: FLEX – FLuorescence EXplorer, published by
ESA Communication Production Office, Noordwijk, the Netherlands, available at:
http://esamultimedia.esa.int/docs/SP1313-4_FLEX.pdf (last access: 13 April 2013), 2008.
10 3906

Fell, F. and Fischer, J.: Numerical simulation of the light field in the atmosphere–ocean system
using the matrix–operator method, J. Quant. Spectrosc. Ra., 69, 351–388, 2001. 3892

Flexas, J., Escalona, J. M., Evain, S., Gulías, J., Moya, I., Osmond, C. B., and Medrano, H.:
Steady-state chlorophyll fluorescence (Fs) measurements as a tool to follow variations of
15 net CO₂ assimilation and stomatal conductance during water-stress in C₃ plants, Physiol.
Plantarum, 114, 231–240, 2002. 3885

Fournier, A., Daumard, F., Champagne, S., Ounis, A., Goulas, Y., and Moya, I.: Effect of canopy
structure on sun-induced chlorophyll fluorescence, ISPRS J. Photogramm., 68, 112–120,
doi:10.1016/j.isprsjprs.2012.01.003, 2012. 3891

20 Frankenberg, C., Butz, A., and Toon, G. C.: Disentangling chlorophyll fluorescence from atmo-
spheric scattering effects in O₂ A-band spectra of reflected sun-light, Geophys. Res. Lett.,
38, L03801, doi:10.1029/2010GL045896, 2011a. 3886, 3900

Frankenberg, C., Fisher, J. B., Worden, J., Badgley, G., Saatchi, S. S., Lee, J.-E., Toon, G. C.,
Butz, A., Jung, M., Kuze, A., and Yokota, T.: New global observations of the terrestrial carbon
25 cycle from GOSAT: patterns of plant fluorescence with gross primary productivity, Geophys.
Res. Lett., 38, L17706, doi:10.1029/2011GL048738, 2011b. 3885, 3886

Frankenberg, C., O'Dell, C., Guanter, L., and McDuffie, J.: Remote sensing of near-infrared
chlorophyll fluorescence from space in scattering atmospheres: implications for its retrieval
and interferences with atmospheric CO₂ retrievals, Atmos. Meas. Tech., 5, 2081–2094,
doi:10.5194/amt-5-2081-2012, 2012. 3885

30 Gamon, J. A. and Berry, J. A.: Facultative and constitutive pigment effects on the Photochemical
Reflectance Index (PRI) in sun and shade conifer needles, Israel, J. Plant Sci., 60, in press,
2013. 3886

O₂ A-band fluorescence retrievals

J. Joiner et al.

Title Page

Abstract

Introduction

Conclusions

References

Tables

Figures

◀

▶

◀

▶

Back

Close

Full Screen / Esc

Printer-friendly Version

Interactive Discussion



- Gamon, J. A., Penuelas, J., and Field, C. B.: A narrow-waveband spectral index that tracks diurnal changes in photosynthetic efficiency, *Remote Sens. Environ.*, 41, 35–44, 1992. 3885
- Guanter, L., Alonso, L., Gómez-Chova, L., Amorós-López, J., Vila-Francés, J., and Moreno, J.: Estimation of solar-induced vegetation fluorescence from space measurements, *Geophys. Res. Lett.*, 34, L08401, doi:10.1029/2007GL029289, 2007. 3885, 3886, 3887, 3894
- Guanter, L., Alonso, L., Gómez-Chova, L., Meroni, M., Preusker, R., Fischer, J., and Moreno, J.: Developments for vegetation fluorescence retrieval from spaceborne high-resolution spectrometry in the O₂ A and O₂-B absorption bands, *J. Geophys. Res.*, 115, D19303, doi:10.1029/2009JD013716, 2010. 3887, 3892, 3893, 3906
- Guanter, L., Frankenberg, C., Dudhia, A., Lewis, P. E., Gómez-Dans, J., Kuze, A., Suto, H., and Grainger, R. G.: Retrieval and global assessment of terrestrial chlorophyll fluorescence from GOSAT space measurements, *Remote Sens. Environ.*, 121, 236–251, 2012. 3885, 3886, 3887, 3902
- Guanter, L., Rossini, M., Colombo, R., Meroni, M., Frankenberg, C., Lee, J.-E., and Joiner, J.: Using field spectroscopy to assess the potential of statistical approaches for the retrieval of sun-induced chlorophyll fluorescence from space, *Remote Sens. Environ.*, 133, 52–61, 2013. 3887, 3891, 3899
- Huete, A. R., Didan, K., Miura, T., Rodriguez, E. P., Gao, X., and Ferreira, L. G.: Overview of the radiometric and biophysical performance of the MODIS vegetation indices, *Remote Sens. Environ.*, 83, 195–213, 2002.
- Jacquemoud, S., Verhoef, W., Baret, F., Bacour, C., Zarco-Tejada, P. J., Asner, G. P., Francois, C., and Ustin, S. L.: PROSPECT + SAIL models: a review of use for vegetation characterization, *Remote Sens. Environ.*, 113, S56–S66, 2009. 3893
- Joiner, J., Yoshida, Y., Vasilkov, A. P., Yoshida, Y., Corp, L. A., and Middleton, E. M.: First observations of global and seasonal terrestrial chlorophyll fluorescence from space, *Biogeosciences*, 8, 637–651, doi:10.5194/bg-8-637-2011, 2011. 3885, 3886
- Joiner, J., Yoshida, Y., Vasilkov, A. P., Middleton, E. M., Campbell, P. K. E., Yoshida, Y., Kuze, A., and Corp, L. A.: Filling-in of near-infrared solar lines by terrestrial fluorescence and other geophysical effects: simulations and space-based observations from SCIAMACHY and GOSAT, *Atmos. Meas. Tech.*, 5, 809–829, doi:10.5194/amt-5-809-2012, 2012. 3885, 3886, 3897, 3899
- Lichtenthaler, H. K.: Chlorophyll fluorescence signatures of leaves during the autumnal chlorophyll breakdown, *J. Plant Physiol.*, 131, 101–110, 1987. 3885

O₂ A-band fluorescence retrievals

J. Joiner et al.

Title Page

Abstract

Introduction

Conclusions

References

Tables

Figures

◀

▶

◀

▶

Back

Close

Full Screen / Esc

Printer-friendly Version

Interactive Discussion



- Louis, J., Ounis, A., Ducruet, J.-M., Evain, S., Laurila, T., Thum, T., Aurela, M., Wingsle, G., Alonso, L., Pedros, R., and Moya, I.: Remote sensing of sunlight-induced chlorophyll fluorescence and reflectance of Scots pine in the boreal forest during spring recovery, *Remote Sens. Environ.*, 96, 37–48, 2005. 3885
- 5 Lucht, W., Schaaf, C. B., and Strahler, A. H.: An algorithm for the retrieval of albedo from space using semiempirical BRDF models, *IEEE T. Geosci. Remote*, 38, 977–998, 2000. 3897
- Marquardt, D. W.: An algorithm for least-squares estimation of nonlinear parameters, *J. Soc. Ind. Appl. Math.*, 11, 431–441, 1963. 3896
- Mazzoni, M., Falorni, P., and Del Bianco, S.: Sun-induced leaf fluorescence retrieval in the O₂–B atmospheric absorption band, *Opt. Express*, 10, 7014–7022, 2008. 3887
- 10 Mazzoni, M., Falorni, P., and Verhoef, W.: High-resolution methods for fluorescence retrieval from space, *Opt. Express*, 15, 15649–15663, 2010. 3887, 3891
- Mazzoni, M., Meroni, M., Fortunato, C., Colombo, R., and Verhoef, W.: Retrieval of maize canopy fluorescence and reflectance by spectral fitting in the O₂–A absorption band, *Remote Sens. Environ.*, 124, 72–82, 2012. 3887, 3891
- 15 Meroni, M. and Colombo, R.: Leaf level detection of solar induced chlorophyll fluorescence by means of a subnanometer resolution spectroradiometer, *Remote Sens. Environ.*, 103, 438–448, 2006. 3885
- Meroni, M., Picchi, V., Rossini, M., Cogliati, S., Panigada, C., Nali, C., Lorenzini, G., and Colombo, R.: Leaf level early assessment of ozone injuries by passive fluorescence and photochemical reflectance index, *Int. J. Remote Sens.*, 29, 5409–5422, 2008. 3885
- 20 Meroni, M., Rossini, M., Guanter, L., Alonso, L., Rascher, U., Colombo, R., and Moreno, J.: Remote sensing of solar-induced chlorophyll fluorescence: review of methods and applications, *Remote Sens. Environ.*, 113, 2037–2051, 2009. 3886
- 25 Meroni, M., Busetto, L., Colombo, R., Guanter, L., Moreno, J., and Verhoef, W.: Performance of spectral fitting methods for vegetation fluorescence quantification, *Remote Sens. Env.*, 114, 363–374, 2010.
- Middleton, E. M., Corp, L. A., and Campbell, P. K. E.: Comparison of measurements and FluorMOD simulations for solar induced chlorophyll fluorescence and reflectance of a corn crop under nitrogen treatments, *Intl. J. Rem. Sensing, Special Issue for the Second International Symposium on Recent Advances in Quantitative Remote Sensing (RAQRSII)*, 29, 5193–5213, 2008. 3885
- 30

O₂ A-band fluorescence retrievals

J. Joiner et al.

Title Page

Abstract

Introduction

Conclusions

References

Tables

Figures

◀

▶

◀

▶

Back

Close

Full Screen / Esc

Printer-friendly Version

Interactive Discussion



- Middleton, E. M., Cheng, Y.-B., Corp, L. A., Huemmrich, K. F., Campbell, P. K. E., Zhang, Q.-Y., Kustas, W. P., and Russ, A. L.: Diurnal and seasonal dynamics of canopy-level solar-induced chlorophyll fluorescence and spectral reflectance indices in a cornfield, in: Proc. 6th EARSeL SIG Workshop on Imaging Spectroscopy, Tel-Aviv, Israel, 16–19 March, CD-Rom, 12 pp., 2009. 3885
- 5 Miller, J. R., Berger, M., Goulas, Y., Jacquemoud, S., Louis, J., Moise, N., Mohammed, G., Moreno, J., Moya, I., Pedrós, R., Verhoef, W., and Zarco-Tejada, P. J.: Development of a Vegetation Fluorescence Canopy Model, ESTEC Contract No. 16365/02/NL/FF, Final Report, 2005. 3893
- 10 Munro, R., Eisinger, M., Anderson, C., Callies, J., Corpaccioli, E., Lang, R., Lefebvre, A., Livschitz, Y., and Perez Albinana, A.: GOME-2 on MetOp: from In-Orbit Verification to Routine Operations, in: Proceedings of EUMETSAT Meteorological Satellite Conference, Helsinki, Finland, 12–16 June 2006. 3888
- 15 Pedrós, R., Goulas, Y., Jacquemoud, S., Louis, J., and Moya, I.: FluorMODleaf: a new leaf fluorescence emission model based on the PROSPECT model, *Remote Sens. Environ.*, 114, 155–167, 2010. 3893
- Plascyk, J. A. and Gabriel, F. C.: The Fraunhofer Line Discriminator MKII – an airborne instrument for precise and standardized ecological luminescence measurement, *IEEE T. Instrum. Meas.*, 24, 306–313, 1975. 3886
- 20 O'Dell, C. W., Connor, B., Bösch, H., O'Brien, D., Frankenberg, C., Castano, R., Christi, M., Eldering, D., Fisher, B., Gunson, M., McDuffie, J., Miller, C. E., Natraj, V., Oyafuso, F., Polonsky, I., Smyth, M., Taylor, T., Toon, G. C., Wennberg, P. O., and Wunch, D.: The ACOS CO₂ retrieval algorithm – Part 1: Description and validation against synthetic observations, *Atmos. Meas. Tech.*, 5, 99–121, doi:10.5194/amt-5-99-2012, 2012. 3894
- 25 Preusker, R. and Lindstrot, R.: Remote sensing of cloud-top pressure using moderately resolved measurements within the oxygen A band – a sensitivity study, *J. Appl. Meteorol. Clim.*, 48, 1562–1574, 2009. 3892, 3893
- Rascher, U.: FLEX – Fluorescence EXplorer: a remote sensing approach to quantify spatio-temporal variations of photosynthetic efficiency from space, *Photosynth. Res.*, 91, 293–294, 2007. 3906
- 30 Rascher, U., Agati, G., Alonso, L., Cecchi, G., Champagne, S., Colombo, R., Damm, A., Daumard, F., de Miguel, E., Fernandez, G., Franch, B., Franke, J., Gerbig, C., Gioli, B., Gómez, J. A., Goulas, Y., Guanter, L., Gutiérrez-de-la-Cámara, Ó., Hamdi, K., Hostert, P.,

O₂ A-band fluorescence retrievals

J. Joiner et al.

Title Page

Abstract

Introduction

Conclusions

References

Tables

Figures

◀

▶

◀

▶

Back

Close

Full Screen / Esc

Printer-friendly Version

Interactive Discussion

Jiménez, M., Kosvancova, M., Lognoli, D., Meroni, M., Miglietta, F., Moersch, A., Moreno, J., Moya, I., Neining, B., Okujeni, A., Ounis, A., Palombi, L., Raimondi, V., Schickling, A., Sobrino, J. A., Stellmes, M., Toci, G., Toscano, P., Udelhoven, T., van der Linden, S., and Zaldei, A.: CEFLES2: the remote sensing component to quantify photosynthetic efficiency from the leaf to the region by measuring sun-induced fluorescence in the oxygen absorption bands, *Biogeosciences*, 6, 1181–1198, doi:10.5194/bg-6-1181-2009, 2009. 3885

Rothman, L. S., Gordon, I. E., Barbe, A., Benner, D. C., Bernath, P. F., Birk, M., Boudon, V., Brown, L. R., Campargue, A., Champion, J., Chance, K., Coudert, L. H., Dana, V., Devi, V. M., Fally, S., Flaud, J. M., Gamache, R. R., Goldman, A., Jacquemart, D., Kleiner, I., Lacombe, N., Lafferty, W. J., Mandin, J., Massie, S. T., Mikhailenko, S. N., Miller, C. E., Moazzen-Ahmadi, N., Naumenko, O. V., Nikitin, A. V., Orphal, J., Perevalov, V. I., Perrin, A., Predoi-Cross, A., Rinsland, C. P., Rotger, M., Simecková, M., Smith, M. A. H., Sung, K., Tashkun, S. A., Tennyson, J., Toth, R. A., Vandaele, A. C., and Vander Auwera, J.: The HITRAN 2008 molecular spectroscopic database, *J. Quant. Spectrosc. Ra.*, 110, 533–572, 2009. 3892

Saito, Y., Kanoh, M., Hatake, K., Kawahara, T. D., and Nomura, A.: Investigation of laser-induced fluorescence of several natural leaves for application to lidar vegetation monitoring, *Appl. Optics*, 37, 431–437, 1998. 3885

Subhash, N. and Mohanan, C. N.: Curve-fit analysis of chlorophyll fluorescence spectra: application to nutrient stress detection in sunflower, *Remote Sens. Environ.*, 60, 347–356, 1997. 3891

van der Tol, C., Verhoef, W., and Rosema, A.: A model for chlorophyll fluorescence and photosynthesis at leaf scale, *Agr. Forest Meteorol.*, 149, 96–105, 2009. 3885

Vasilkov, A., Joiner, J., and Spurr, R.: Note on rotational-Raman scattering in the O₂ A- and B-bands, *Atmos. Meas. Tech.*, 6, 981–990, doi:10.5194/amt-6-981-2013, 2013. 3892, 3894

Veefkind, J. P., Aben, I., McMullan, K., Forster, H., de Vries, J., Otter, G., Claas, J., Eskes, H. J., de Haan, J. F., Kleipool, Q., van Weele, M., Hasekamp, O., Hoogeveen, R., Landgraf, J., Snel, R., Tol, P., Ingmann, P., Voors, R., Kruizinga, B., Vink, R., Visser, H., and Levelt, P. F.: TROPOMI on the ESA Sentinel-5 Precursor: a GMES mission for global observations of the atmospheric composition for climate, air quality and ozone layer applications, *Remote Sens. Environ.*, 120, 70–83, doi:10.1016/j.rse.2011.09.027, 2012. 3906

**O₂ A-band
fluorescence
retrievals**

J. Joiner et al.

Title Page

Abstract

Introduction

Conclusions

References

Tables

Figures



Back

Close

Full Screen / Esc

Printer-friendly Version

Interactive Discussion



Zarco-Tejada, P. J., Miller, J. R., Mohammed, G. H., and Noland, T. L.: Chlorophyll fluorescence effects on vegetation apparent reflectance: I. Leaf-level measurements and model simulations, *Remote Sens. Environ.*, 74, 582–595, 2000. 3891

5 Zarco-Tejada, P. J., Berni, J. A. J., Suarez, L., Sepulcre-Cantó, G., Morales, F., and Miller, J. R.: Imaging chlorophyll fluorescence with an airborne narrow-band multispectral camera for vegetation stress detection, *Remote Sens. Environ.*, 113, 1262–1275, 2009. 3885

10 Zarco-Tejada, P. J., Morales, A., Testi, L., and Villalobos, F. J.: Spatio-temporal patterns of chlorophyll fluorescence and physiological and structural indices acquired from hyperspectral imagery as compared with carbon fluxes measured with eddy covariance, *Remote Sens. Environ.*, 133, 102–115, 2013. 3885

O₂ A-band fluorescence retrievals

J. Joiner et al.

Table 1. Statistical comparison of retrieved versus true values of I_F obtained using simulated data; all fluorescence radiance units are $\text{mW m}^{-2} \text{nm}^{-1} \text{sr}^{-1}$.

Exp	FWHM	SNR	#PCs	λ_1 (nm)	λ_2 (nm)	RMS diff.	r	mean diff.	σ	slope	intercept
1	0.5 nm	2000	5	747	780	0.88	0.67	-0.68	0.57	0.43	-0.03
2	0.5 nm	2000	10	747	780	0.58	0.82	-0.37	0.45	0.58	0.11
3	0.5 nm	2000	15	747	780	0.50	0.87	-0.32	0.38	0.72	-0.01
4	0.5 nm	2000	25	747	780	0.43	0.87	-0.22	0.38	0.80	0.01
5	0.5 nm	1000	25	747	780	0.70	0.69	-0.22	0.67	0.80	0.01
6	0.5 nm	2000	25	712	747	0.33	0.97	-0.07	0.32	1.00	0.07
7	0.5 nm	2000	25	723	747	0.37	0.97	-0.01	0.37	0.94	0.13
8	0.5 nm	2000	25	755	775	0.56	0.76	-0.30	0.47	0.71	0.01
9	0.5 nm	2000	25	759	768	1.19	0.43	-0.46	1.10	0.70	-0.13
6	0.5 nm	2000	25	747	758	1.48	0.58	-0.03	1.48	0.98	0.01
11	0.3 nm	2000	25	747	780	0.49	0.85	-0.29	0.40	0.80	-0.06
12	0.3 nm	2000	25	712	747	0.22	0.99	-0.11	0.19	0.94	0.02

Title Page

Abstract

Introduction

Conclusions

References

Tables

Figures

◀

▶

◀

▶

Back

Close

Full Screen / Esc

Printer-friendly Version

Interactive Discussion



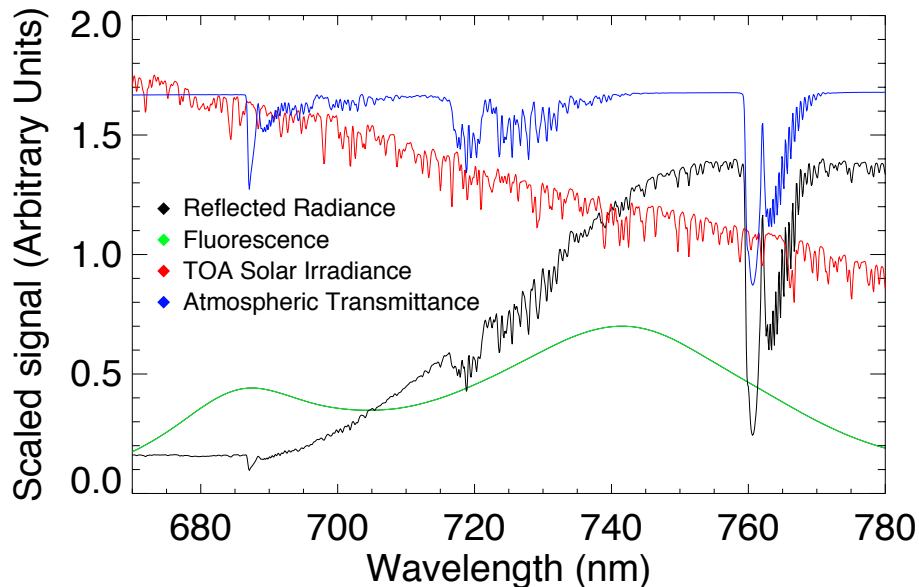


Fig. 1. Simulated solar-induced terrestrial fluorescence, typical simulated atmospheric transmittance and reflectance, and solar irradiance as a function of wavelength computed for an instrument with FWHM = 0.3 nm. The fluorescence shows red and far-red chlorophyll emission features with peaks near 685 and 740 nm, respectively. Oxygen A and B absorption bands are located near 687 and 760 nm, respectively, while water vapor absorption is shown over a broad spectral range between about 690 and 740 nm. The solar irradiance shows weak solar Fraunhofer line structure at this spectral resolution.

**O₂ A-band
fluorescence
retrievals**

J. Joiner et al.

Title Page

Abstract

Introduction

Conclusions

References

Tables

Figures

◀

▶

◀

▶

Back

Close

Full Screen / Esc

Printer-friendly Version

Interactive Discussion



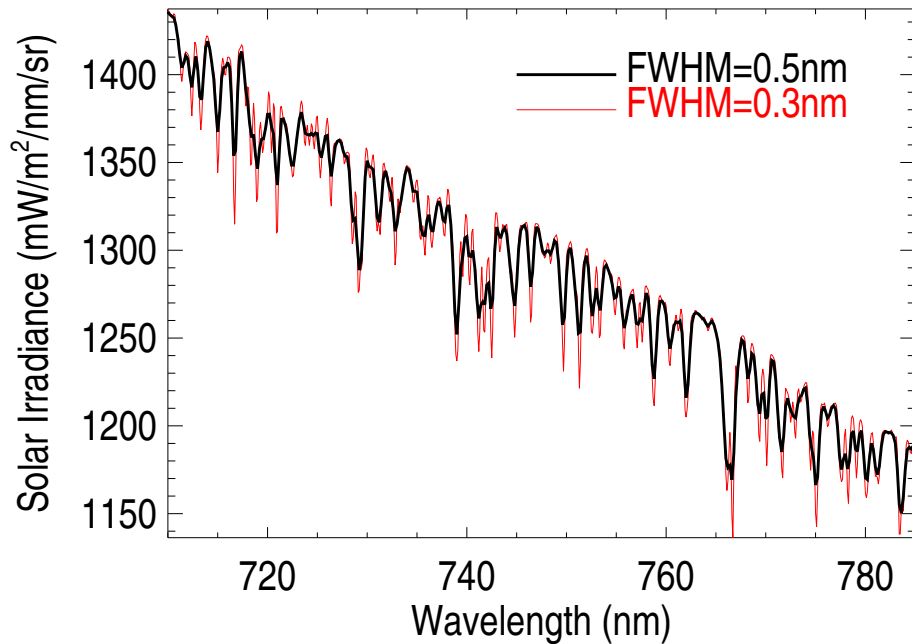


Fig. 2. Simulated solar spectra based on Chance and Kurucz (2010) for different instrumentation showing Fraunhofer line structure (FWHM = 0.5 nm is for a GOME-2-like instrument).

**O₂ A-band
fluorescence
retrievals**

J. Joiner et al.

Title Page	
Abstract	Introduction
Conclusions	References
Tables	Figures
◀	▶
◀	▶
Back	Close
Full Screen / Esc	
Printer-friendly Version	
Interactive Discussion	



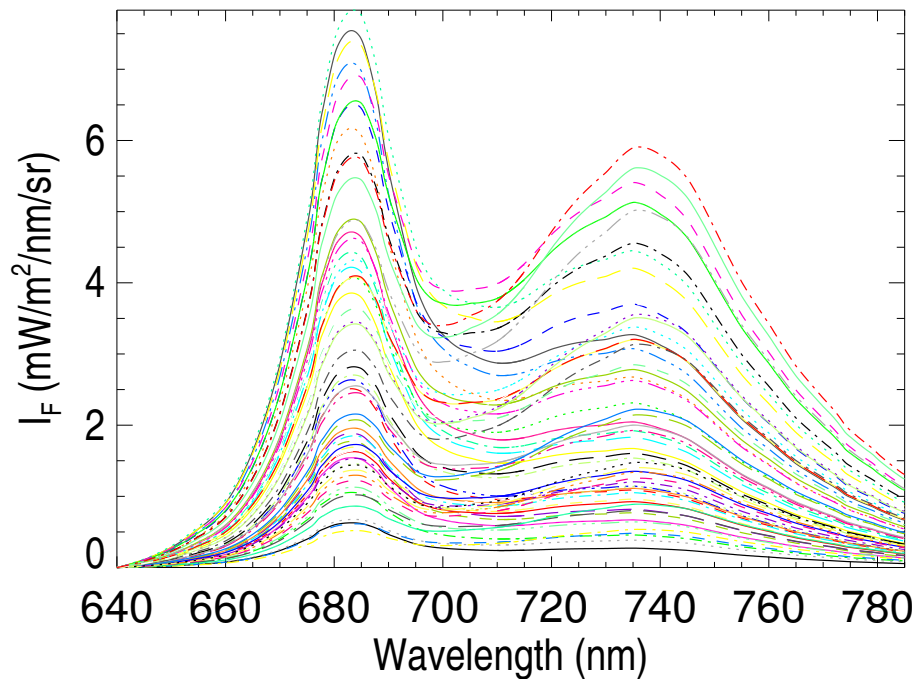


Fig. 3. Canopy-level spectral fluorescence as specified for the range of conditions in the simulated data set.

**O₂ A-band
fluorescence
retrievals**

J. Joiner et al.

Title Page

Abstract

Introduction

Conclusions

References

Tables

Figures

◀

▶

◀

▶

Back

Close

Full Screen / Esc

Printer-friendly Version

Interactive Discussion



O₂ A-band fluorescence retrievals

J. Joiner et al.

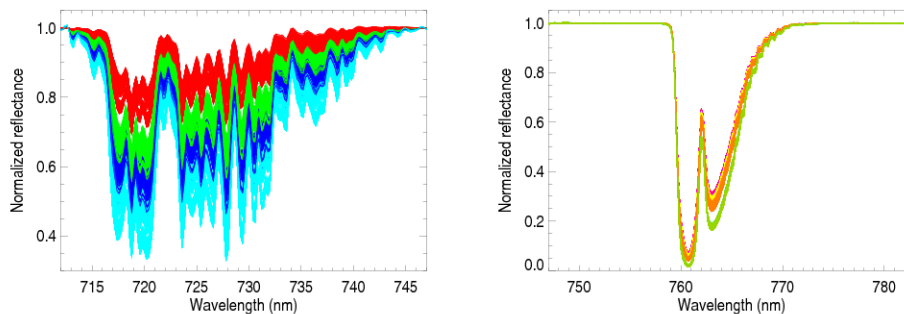


Fig. 4. Transmittances derived from the training data set. The different colors in the left panel correspond to different values of total column water vapor; colors on right panel correspond to different combinations of solar and viewing zenith angles.

[Title Page](#)[Abstract](#)[Introduction](#)[Conclusions](#)[References](#)[Tables](#)[Figures](#)[◀](#)[▶](#)[◀](#)[▶](#)[Back](#)[Close](#)[Full Screen / Esc](#)[Printer-friendly Version](#)[Interactive Discussion](#)

O₂ A-band
fluorescence
retrievals

J. Joiner et al.

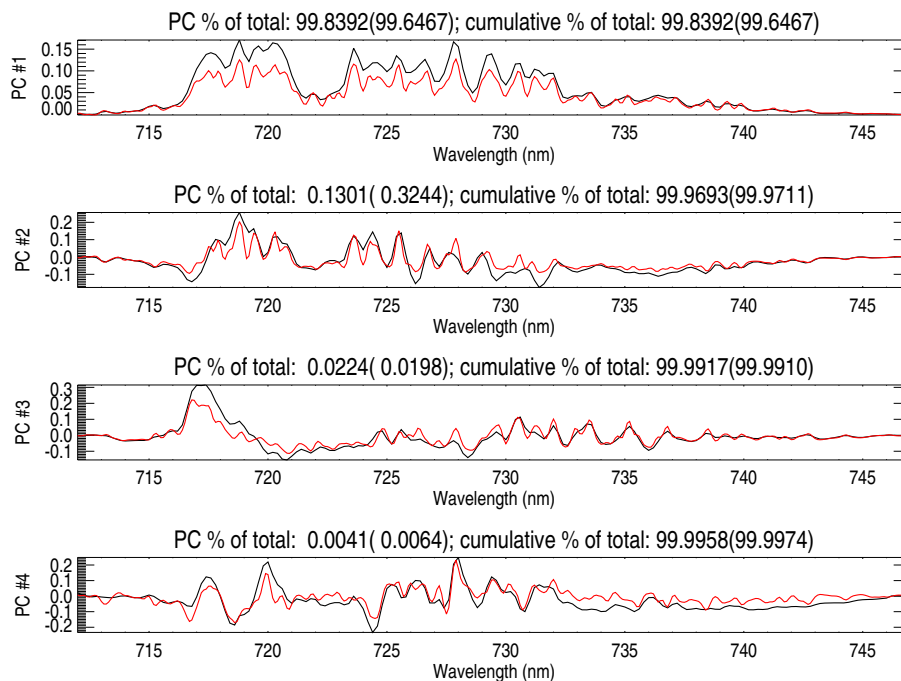


Fig. 5. Leading principal components (PCs) of simulated reflectance spectra for the short wavelength fitting window for a GOME-like instrument with FWHM = 0.5 nm (black) and a higher spectral resolution instrument with FWHM = 0.3 nm (red); numbers in the top title are the variance explained in terms of percent of the total and cumulative percent of the total with numbers for FWHM = 0.3 nm in parentheses.

Title Page

Abstract

Introduction

Conclusions

References

Tables

Figures

◀

▶

◀

▶

Back

Close

Full Screen / Esc

Printer-friendly Version

Interactive Discussion



**O₂ A-band
fluorescence
retrievals**

J. Joiner et al.

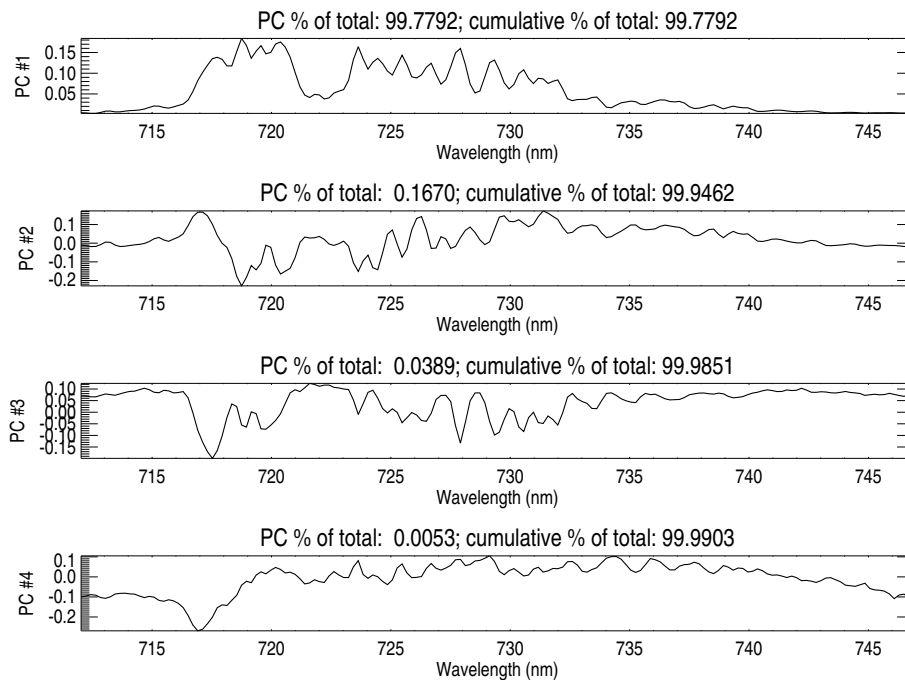


Fig. 6. Similar to Fig. 5 but the PCA is conducted using actual GOME-2 data taken over ice- and snow-covered surfaces, the Sahara desert, and cloudy ocean.

[Title Page](#)[Abstract](#)[Introduction](#)[Conclusions](#)[References](#)[Tables](#)[Figures](#)[◀](#)[▶](#)[◀](#)[▶](#)[Back](#)[Close](#)[Full Screen / Esc](#)[Printer-friendly Version](#)[Interactive Discussion](#)

O₂ A-band fluorescence retrievals

J. Joiner et al.

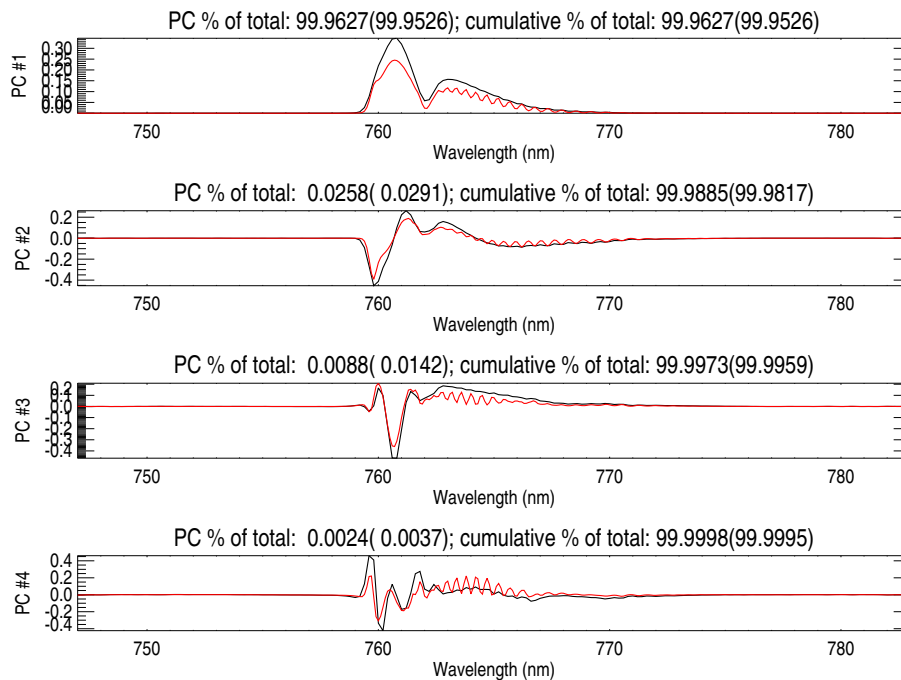


Fig. 7. Similar to Fig. 5 but for the long wavelength fitting window.

[Title Page](#)[Abstract](#)[Introduction](#)[Conclusions](#)[References](#)[Tables](#)[Figures](#)[◀](#)[▶](#)[◀](#)[▶](#)[Back](#)[Close](#)[Full Screen / Esc](#)[Printer-friendly Version](#)[Interactive Discussion](#)

**O₂ A-band
fluorescence
retrievals**

J. Joiner et al.

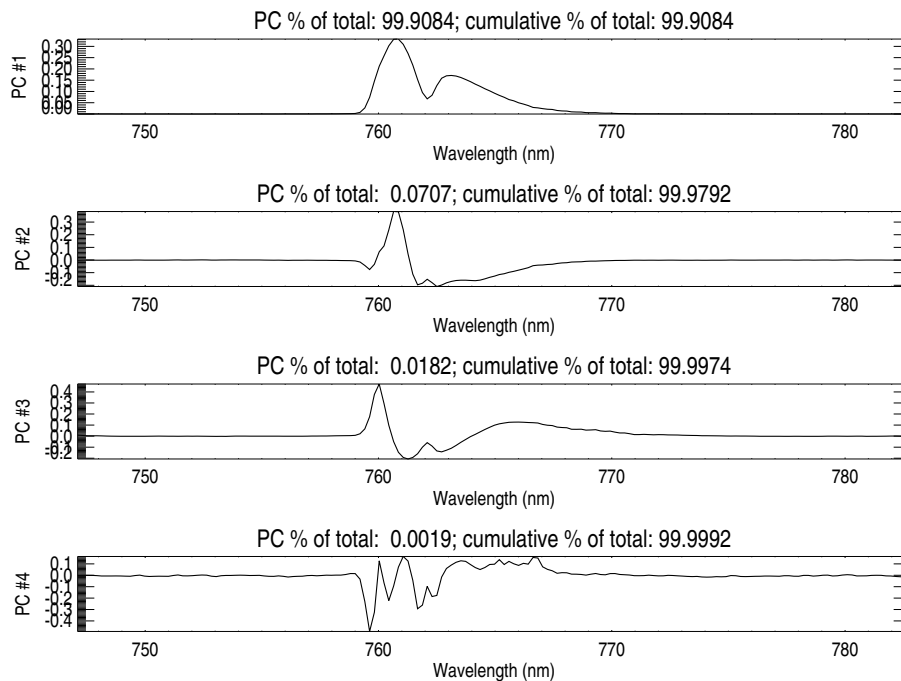


Fig. 8. Similar to Fig. 6 but for the long wavelength fitting window computed using actual GOME-2 data.

[Title Page](#)[Abstract](#)[Introduction](#)[Conclusions](#)[References](#)[Tables](#)[Figures](#)[◀](#)[▶](#)[◀](#)[▶](#)[Back](#)[Close](#)[Full Screen / Esc](#)[Printer-friendly Version](#)[Interactive Discussion](#)

O₂ A-band fluorescence retrievals

J. Joiner et al.

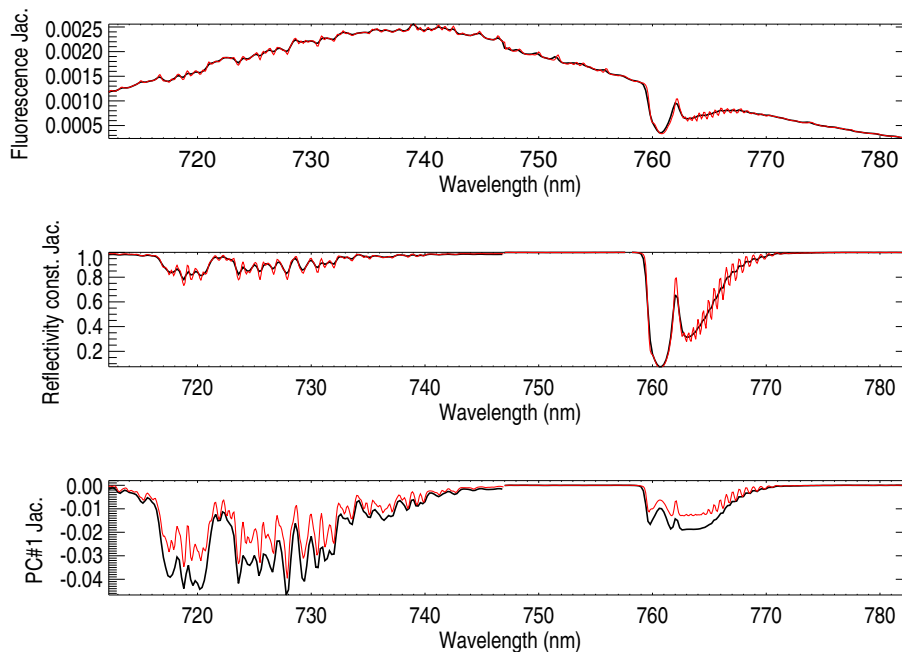


Fig. 9. Typical Jacobians ($\partial\rho/\partial x$) where x is the far-red fluorescence peak value (top), the wavelength-independent component of the surface reflectivity (middle), and the coefficient of the first PC (bottom) for FWHM = 0.5 nm (black) and FWHM = 0.3 nm (red). The PC analyses are carried out separately for the wavelength ranges 712–747 nm and 747–783 nm but are shown in a single plot for convenience.

[Title Page](#)[Abstract](#)[Introduction](#)[Conclusions](#)[References](#)[Tables](#)[Figures](#)[◀](#)[▶](#)[◀](#)[▶](#)[Back](#)[Close](#)[Full Screen / Esc](#)[Printer-friendly Version](#)[Interactive Discussion](#)

**O₂ A-band
fluorescence
retrievals**

J. Joiner et al.

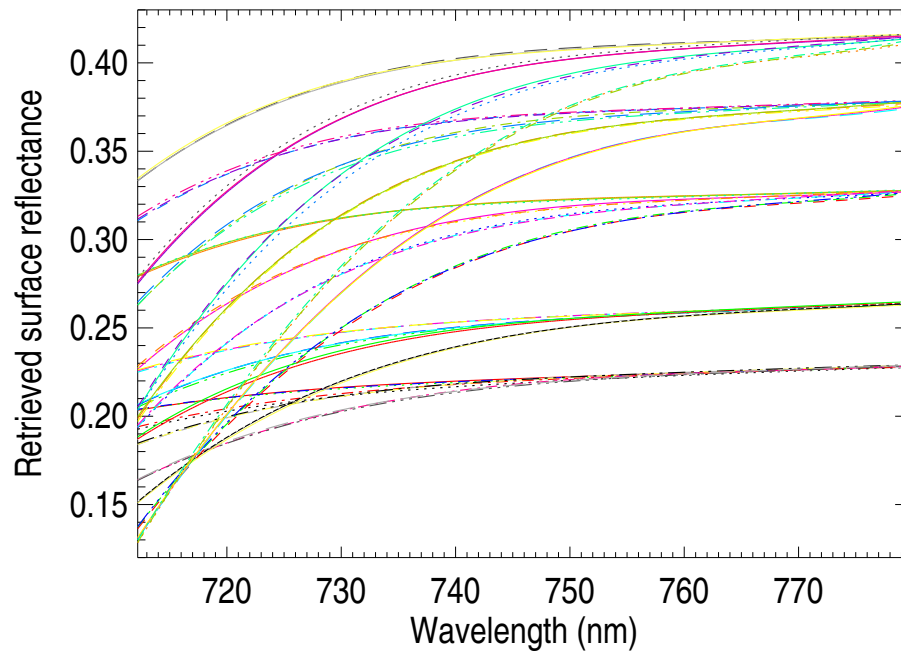


Fig. 10. Retrieved spectral surface reflectances for the range of conditions in the simulated data set.

Title Page

Abstract

Introduction

Conclusions

References

Tables

Figures

◀

▶

◀

▶

Back

Close

Full Screen / Esc

Printer-friendly Version

Interactive Discussion



O₂ A-band fluorescence retrievals

J. Joiner et al.

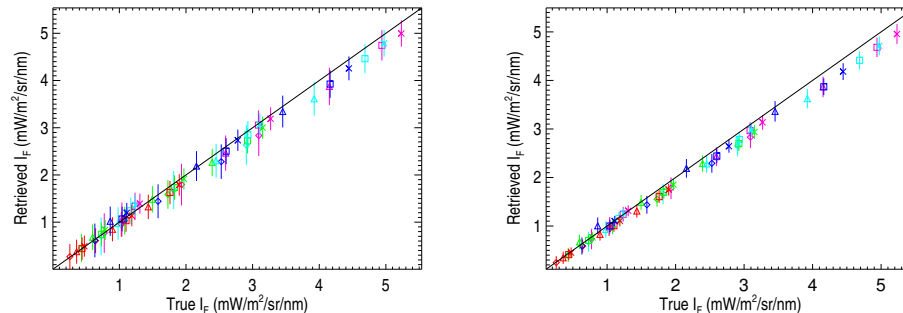


Fig. 11. Fluorescence retrievals from simulated data (y-axis) using wavelengths between 712 and 747 nm for instruments with FWHM = 0.5 nm (left) and FWHM = 0.3 nm (right). Fluorescence is averaged over the wavelengths used in the retrieval and compared with the “truth” (x-axis) averaged in the same way. Standard deviations are shown with vertical bars. Different symbols are shown for the various values of chlorophyll content and different colors are for the different values of leaf area index.

[Title Page](#)[Abstract](#)[Introduction](#)[Conclusions](#)[References](#)[Tables](#)[Figures](#)[◀](#)[▶](#)[◀](#)[▶](#)[Back](#)[Close](#)[Full Screen / Esc](#)[Printer-friendly Version](#)[Interactive Discussion](#)

**O₂ A-band
fluorescence
retrievals**

J. Joiner et al.

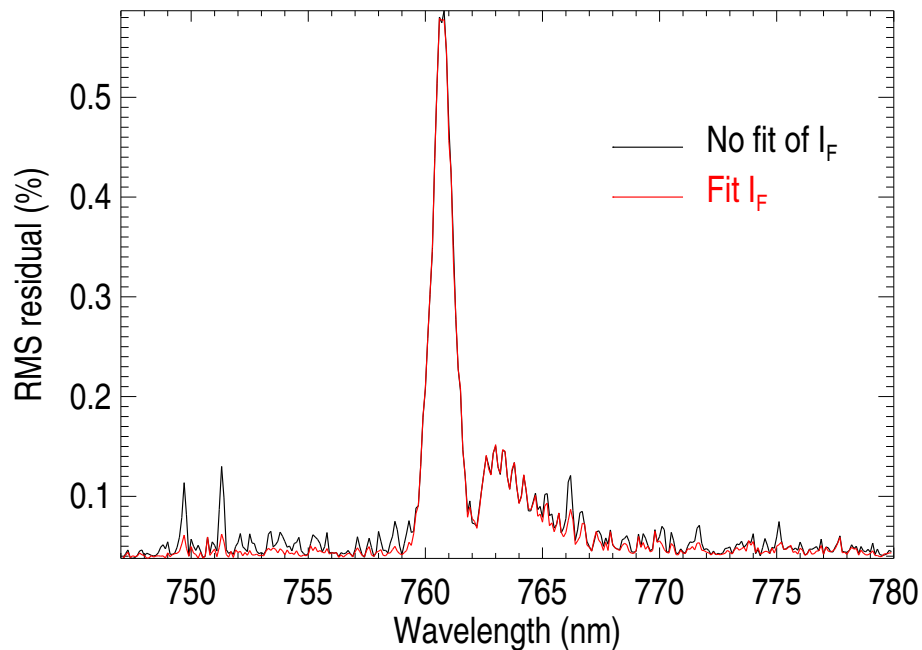


Fig. 12. RMS of simulated radiance residuals (in percent of radiance) from testing dataset with FWHM = 0.3 nm and SNR = 2000 when fluorescence radiance (I_F) is fit/retrieved and when it is not fit/retrieved.

Title Page

Abstract

Introduction

Conclusions

References

Tables

Figures

◀

▶

◀

▶

Back

Close

Full Screen / Esc

Printer-friendly Version

Interactive Discussion



**O₂ A-band
fluorescence
retrievals**

J. Joiner et al.

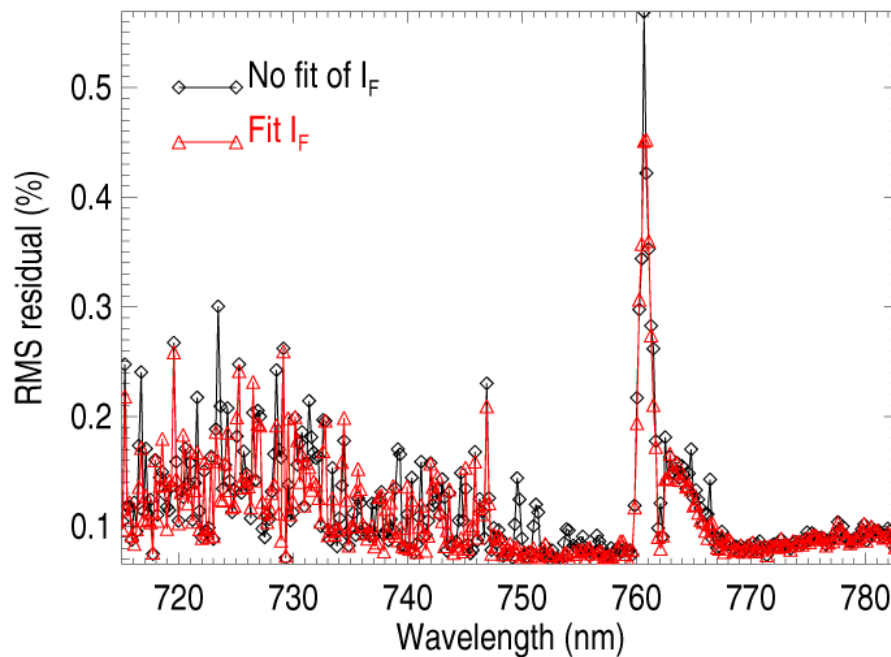


Fig. 13. RMS of GOME-2 radiance residuals (in percent of the observed radiance) for a single day for moderately to highly vegetated pixels.

Title Page

Abstract

Introduction

Conclusions

References

Tables

Figures

◀

▶

◀

▶

Back

Close

Full Screen / Esc

Printer-friendly Version

Interactive Discussion



O₂ A-band fluorescence retrievals

J. Joiner et al.

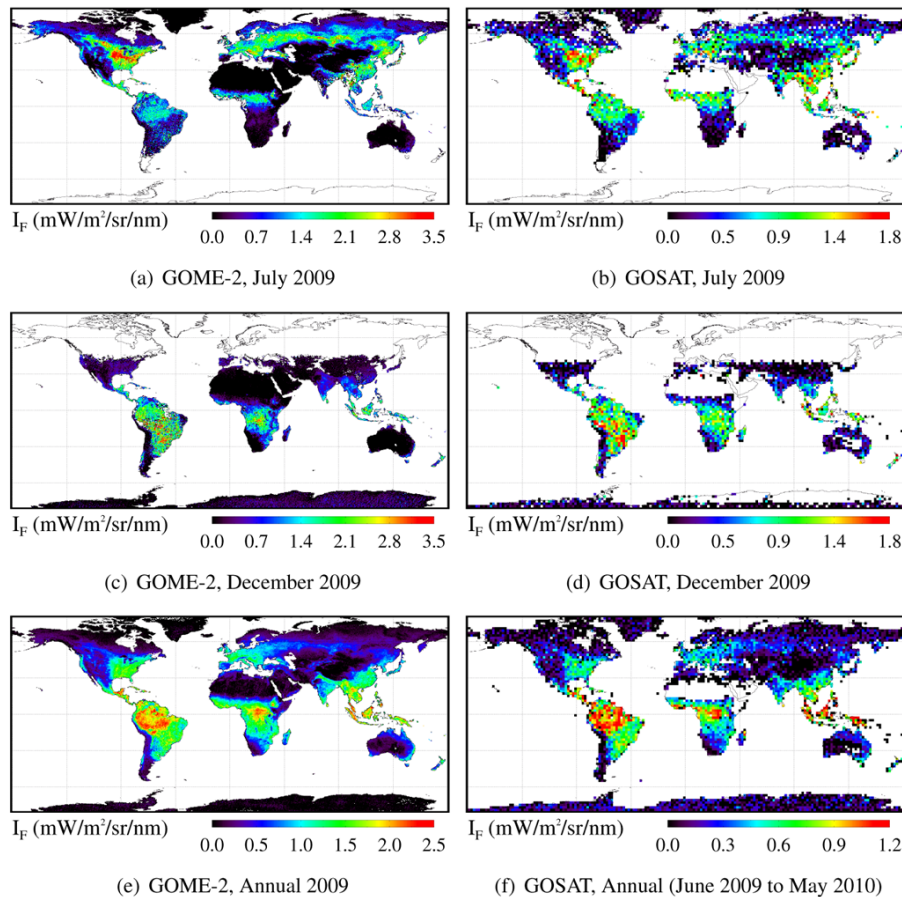


Fig. 14. Global composites of I_F from GOME-2 and GOSAT-FTS retrievals for July, December and the annual average in 2009 (June 2009 through May 2010 for GOSAT). GOME-2 retrievals are referred to 737 nm and binned in 0.5° cell boxes; GOSAT retrievals are performed at 755 nm and binned in 2° cell boxes.

Title Page

Abstract

Introduction

Conclusions

References

Tables

Figures

◀

▶

◀

▶

Back

Close

Full Screen / Esc

Printer-friendly Version

Interactive Discussion



O₂ A-band fluorescence retrievals

J. Joiner et al.

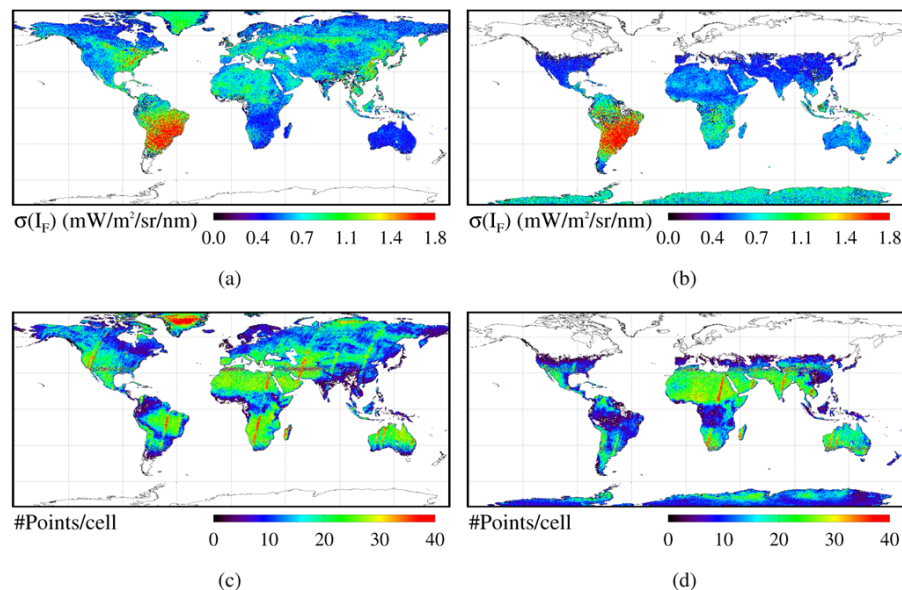


Fig. 15. Global maps of GOME-2 I_F retrieval statistical parameters in a 0.5° grid cell for July (left column) and December (right column) 2009. Each column shows the standard deviation (top) and the number of points per grid cell (bottom).

Title Page

Abstract

Introduction

Conclusions

References

Tables

Figures

◀

▶

◀

▶

Back

Close

Full Screen / Esc

Printer-friendly Version

Interactive Discussion



O₂ A-band fluorescence retrievals

J. Joiner et al.

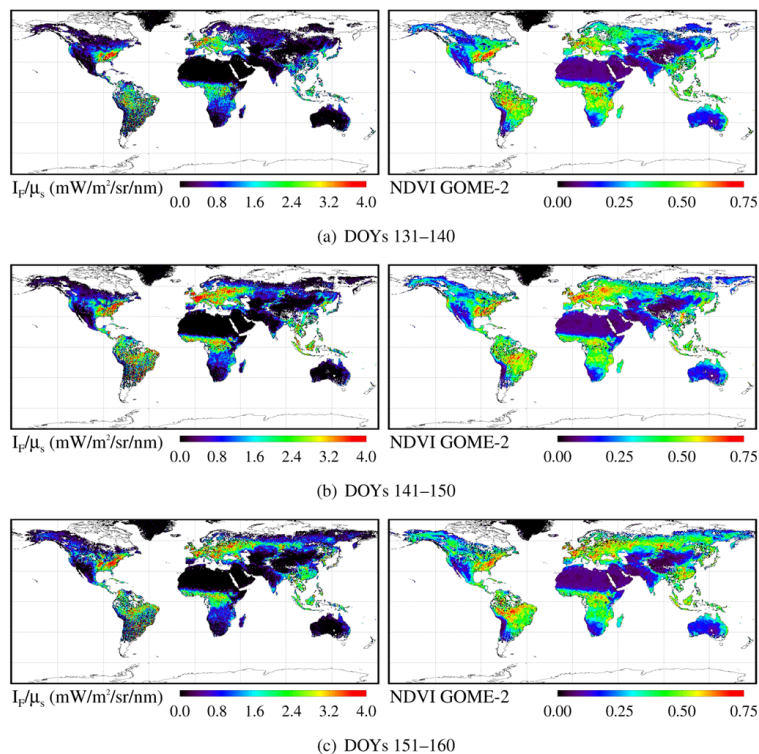


Fig. 16. 10 day composites of I_F and NDVI derived from GOME-2 data between day-of-year (DOY) 131 and 160 of 2009. Fluorescence is normalized by the cosine of the sun zenith angle (μ_s) in order to minimize the temporal and latitudinal dependence of fluorescence on incoming at-surface photosynthetically-active radiation.

Title Page

Abstract

Introduction

Conclusions

References

Tables

Figures

◀

▶

◀

▶

Back

Close

Full Screen / Esc

Printer-friendly Version

Interactive Discussion

